

A Physics-Driven AI Approach for Microwave Imaging of Breast Tumors

F. Zardi,⁽¹⁾⁽²⁾ *Member, IEEE*, L. Tosi,⁽¹⁾⁽²⁾ *Member, IEEE*, M. Salucci,⁽¹⁾⁽²⁾ *Senior Member, IEEE*, and A. Massa,⁽¹⁾⁽²⁾⁽³⁾⁽⁴⁾⁽⁵⁾ *Fellow, IEEE*

⁽¹⁾ *ELEDIA Research Center (ELEDIA@UniTN - University of Trento)*

DICAM - Department of Civil, Environmental, and Mechanical Engineering

Via Mesiano 77, 38123 Trento - Italy

E-mail: {francesco.zardi, luca.tosi, marco.salucci, andrea.massa}@unitn.it

Website: www.eledia.org/eledia-unitn

⁽²⁾ *CNIT - "University of Trento" ELEDIA Research Unit*

Via Sommarive 9, 38123 Trento - Italy

Website: www.eledia.org/eledia-unitn

⁽³⁾ *ELEDIA Research Center (ELEDIA@UESTC - UESTC)*

School of Electronic Science and Engineering, Chengdu 611731 - China

E-mail: andrea.massa@uestc.edu.cn

Website: www.eledia.org/eledia-uestc

⁽⁴⁾ *ELEDIA Research Center (ELEDIA@TSINGHUA - Tsinghua University)*

30 Shuangqing Rd, 100084 Haidian, Beijing - China

E-mail: andrea.massa@tsinghua.edu.cn

Website: www.eledia.org/eledia-tsinghua

⁽⁵⁾ *School of Electrical Engineering*

Tel Aviv University, Tel Aviv 69978 - Israel

E-mail: andrea.massa@eng.tau.ac.il

Website: <https://engineering.tau.ac.il/>

This work has been submitted to the IEEE for possible publication. Copyright may be transferred without notice, after which this version may no longer be accessible.

A Physics-Driven AI Approach for Microwave Imaging of Breast Tumors

F. Zardi, L. Tosi, M. Salucci, and A. Massa

Abstract

In this paper, an innovative microwave imaging (*MI*) approach for breast tumor diagnosis is proposed that employs a differential formulation of the inverse scattering problem (*ISP*) at hand to exploit arbitrary-fidelity *priors* on the inhomogeneous reference/healthy tissues. The quantitative imaging of the unknown tumor is then rephrased into a global optimization problem, which is efficiently solved with an *ad-hoc* physics-driven artificial intelligence (*AI*) strategy inspired by the concepts and guidelines of the System-by-Design (*SbD*) paradigm. The effectiveness, the robustness, the reliability, and the efficiency of the proposed method are assessed against both synthetic and experimental data.

Key words: Inverse Scattering Problem (*ISP*), Microwave Imaging (*MI*), Breast Imaging, Artificial Intelligence (*AI*), System-by-Design (*SbD*), Learning-by-Examples (*LBE*), Evolutionary Algorithms (*EAs*).

1 Introduction

As claimed by the World Health Organization, breast tumor is nowadays the most diffused cancer in the world with over 2 million cases reported during the year 2020 [1]. Recent studies have shown that early diagnosis through mammography screening leads to a substantial decrease in mortality [2]. However, the screening systems currently-in-use, which are based on magnetic resonance imaging (*MRI*) and X-ray technology, present several drawbacks such as the need for complex and expensive equipment with limited availability that hinders regular mass screening programs. In addition, the use of either injected contrast liquids or ionizing radiation raises non-negligible concerns on the potential health implications of a regular/repeated examination with these modalities [3].

Alternatively, microwave imaging (*MI*) is an emerging and promising solution to overcome such limitations [4]. In *MI*, the breast is illuminated with non-ionizing electromagnetic (*EM*) waves and the arising scattering response is processed to determine qualitative (e.g., the presence, the position, and the shape) and/or quantitative (e.g., the permittivity and the conductivity distributions) information on the diagnosed tissues. From a practical point of view, the equipment for collecting the microwave data is relatively inexpensive and it can be designed with compact (i.e., portable) form factors [5] or even embedded in wearable devices [6]. Moreover, current *MI* systems support quite expedite data collection processes, in the range of a few seconds [7]. On the other hand, detecting and retrieving the features of abnormal (tumoral) tissues from *EM* field measurements requires the solution of an inverse scattering problem (*ISP*) and, therefore, to effectively/efficiently cope with several paramount challenges [8].

As a matter of fact, *ISPs* are generally ill-posed, which means that (i) more than one solution exists since different dielectric distributions could match the same scattering data and that (ii) the *MI* solution does not continuously depend on these latter [8]. Such an issue can be mitigated by including some *a-priori* information on the imaged scenario, on its underlying physics, and on the type and nature of the unknowns to integrate the information content of the scattering data. For instance, a differential formulation of the *ISP* is an effective regularization recipe since the unknown is no more the complete distribution of the investigation domain, but only the difference with respect to a known dielectric profile [9][10]. As for the *MI* of the breast, such a

reference scenario corresponds to the normal/healthy tissues, which knowledge can be gathered from previous analyses performed with microwave [11]-[15], *MRI* [16][17], or ultrasound [18]-[20] investigations.

Another fundamental challenge of *MI* comes from the non-linear relationship between the *ISP* unknowns and the scattered data [8]. Such an issue can be overcome by adopting linear formulations aimed at retrieving a map of the reflected energy from the breast, rather than its permittivity and conductivity distributions, by means of radar-based strategies [21]-[26]. However, the result is a qualitative imaging of the breast that often does not provide sufficient information to discriminate between benign and malign abnormalities [27] and to monitor the follow-up of an ongoing medical treatment [28]. Similar limitations may occur when counteracting the non-linearity by means of linearized formulations of the scattering equations (e.g., Born's and/or Rytov's approximations [29]-[32]).

Otherwise, fully non-linear quantitative solutions of the *ISP* can be found by means of properly customized deterministic (*DAs*) or stochastic (*SAs*) algorithms. The former class includes local search techniques such as the Conjugate Gradient (*CG*) method [33][34]. They are usually very fast, but they may be trapped into local minima unless the starting solution already belongs to the "attraction basin" of the global optimum. Conversely, *SAs* (e.g., Evolutionary Algorithms (*EA*) [35]-[39]) perform a global search and they are more resilient to the initialization problem thanks to their hill-climbing properties. Unfortunately, the repeated full-wave evaluation of the forward scattering operators to assess the fitness of the trial guess solutions [35] could result in a computation burden not compatible with the goal of a fast medical screening.

Recently, artificial intelligence (*AI*) has emerged as a powerful framework for solving *ISPs* with unprecedented computational efficiency leveraging the Learning-by-Examples (*LBE*) and Deep Learning (*DL*) paradigms [40]-[42]. Such techniques exploit a training set of properly-chosen examples of the input-output relation between unknowns and *ISP* data to build a surrogate model (*SM*) significantly faster than a traditional full-wave solver in predicting the output/data [40]. Clearly, the success of such strategies depends on the ability to generate a minimum-cardinality set of representative training examples, sampling a minimum-dimensionality solution space to cope with the "curse-of-dimensionality" [40][43], thus minimizing the computational effort of

the off-line training phase.

In such a context, this paper presents a novel physics-driven *AI* method for reliably solving fully non-linear microwave breast *ISPs* with a high computational efficiency. Thanks to a differential formulation of the underlying scattering phenomena, which enables the exploitation of arbitrary-fidelity *priors* on the inhomogeneous reference/healthy tissues, a minimum-dimensionality search space is defined and adaptively sampled by means of an *EA*-based global search engine that leverages a *SM* of the cost function to speed-up the inversion, while keeping the same prediction accuracy. The arising inversion strategy, inspired by the concepts and guidelines of the System-by-Design (*SbD*) framework [44], is validated on both synthetic data based on *MRI*-derived numerical phantoms [45] and experimental data [46].

The outline of the work is the following. The formulation of the differential breast *ISP* is detailed in Sect. 2, whereas the *AI*-based *MI* approach is described in Sect. 3. An extensive validation considering different operative conditions and benchmark problems of increasing complexity is reported in Sect. 4. Finally, some conclusions and final remarks are drawn (Sect. 5).

2 Mathematical Formulation of the Breast *ISP*

Let us consider a 2-*D* square investigation domain Ω of side L embedding a coronal slice Λ parallel to the chest wall of the patient's breast [Fig. 1(a)]. The normal (healthy) tissue within Λ is modeled by means of the complex permittivity distribution $\tilde{\varepsilon}_{\mathcal{N}}(\mathbf{r})$ ($\tilde{\varepsilon}_{\mathcal{N}}(\mathbf{r}) \triangleq \varepsilon_0 \varepsilon_{\mathcal{N}}(\mathbf{r}) - j \frac{\sigma_{\mathcal{N}}(\mathbf{r})}{2\pi f}$), $\varepsilon_{\mathcal{N}}(\mathbf{r})$ and $\sigma_{\mathcal{N}}(\mathbf{r})$ being the relative permittivity and the conductivity at the position $\mathbf{r} = (x, y)$, respectively. Moreover, ε_0 is the vacuum permittivity and f is the working frequency⁽¹⁾. Under the hypothesis that Λ includes a tumor, which is modeled as a region with bounded support $\Psi \subset \Lambda$ of abnormal permittivity $\tilde{\varepsilon}_{\mathcal{A}}(\mathbf{r})$ [$\tilde{\varepsilon}_{\mathcal{A}}(\mathbf{r}) \triangleq \varepsilon_0 \varepsilon_{\mathcal{A}}(\mathbf{r}) - j \frac{\sigma_{\mathcal{A}}(\mathbf{r})}{2\pi f}$], the dielectric profile of the region Λ turns out to be

$$\tilde{\varepsilon}(\mathbf{r}) = \begin{cases} \tilde{\varepsilon}_{\mathcal{A}}(\mathbf{r}) & \text{if } \mathbf{r} \in \Psi \\ \tilde{\varepsilon}_{\mathcal{N}}(\mathbf{r}) & \text{if } \mathbf{r} \in (\Lambda - \Psi) \\ \tilde{\varepsilon}_{\mathcal{B}} & \text{otherwise,} \end{cases} \quad (1)$$

⁽¹⁾To simplify the notation, the time dependence $\exp(j2\pi ft)$ is omitted hereinafter.

$\tilde{\varepsilon}_{\mathcal{B}}$ being the permittivity of the homogeneous background medium surrounding the breast [$\tilde{\varepsilon}_{\mathcal{B}} \triangleq \varepsilon_0 \varepsilon_{\mathcal{B}} - j \frac{\sigma_{\mathcal{B}}}{2\pi f}$ - Fig. 1(a)].

The acquisition system is a transverse magnetic (*TM*) multi-view/multi-static setup composed by a set of V antennas located at the positions $\{\mathbf{r}^v \in \Theta; v = 1, \dots, V\}$ in an external circular observation domain Θ of radius ρ_{Θ} [$\Theta \cap \Omega = \emptyset$ - Fig. 1(a)]. Such antennas are alternatively operated in transmit or receive mode so that, when the v -th ($v = 1, \dots, V$) one is transmitting, the remaining $M = (V - 1)$ ones collect the electric field in M different positions $\{\mathbf{r}_m^v \in \Theta; m = 1, \dots, M\}$. In the following, let us denote with $E_{inc}^v(\mathbf{r})$ the incident field associated to the v -th ($v = 1, \dots, V$) probing source radiating in free-space, while $E^v(\mathbf{r})$ stands for the total field due to the *EM* interactions between the v -th ($v = 1, \dots, V$) source and the inhomogeneous distribution (1). These latter can be modeled by means of the *State*,

$$E_{inc}^v(\mathbf{r}) = E^v(\mathbf{r}) - \int_{\Omega} G_{\mathcal{B}}(\mathbf{r}, \mathbf{r}') \tau(\mathbf{r}') E^v(\mathbf{r}') d\mathbf{r}'; \quad \mathbf{r} \in \Omega; v = 1, \dots, V, \quad (2)$$

and the *Data*,

$$S^v(\mathbf{r}_m^v) = \int_{\Omega} G_{\mathcal{B}}(\mathbf{r}_m^v, \mathbf{r}') \tau(\mathbf{r}') E^v(\mathbf{r}') d\mathbf{r}'; \quad \mathbf{r}_m^v \in \Theta; v = 1, \dots, V; m = 1, \dots, M, \quad (3)$$

equations, where $\tau(\mathbf{r})$ [$\tau(\mathbf{r}) \triangleq \frac{\tilde{\varepsilon}(\mathbf{r})}{\tilde{\varepsilon}_{\mathcal{B}}} - 1$] is the actual contrast, $S^v \triangleq (E^v - E_{inc}^v)$ is the v -th ($v = 1, \dots, V$) scattered field, and $G_{\mathcal{B}}$ is the Green's function of the homogeneous background. By observing that the field contribution, $E_{\mathcal{N}}^v(\mathbf{r})$, due to the normal tissue, $\tau_{\mathcal{N}}(\mathbf{r})$ [$\tau_{\mathcal{N}}(\mathbf{r}) \triangleq [\tilde{\varepsilon}_{\mathcal{N}}(\mathbf{r}) / \tilde{\varepsilon}_{\mathcal{B}}] - 1$] can be predicted starting from the available *prior* knowledge of a *Reference Scenario* not including the tumor [Fig. 1(b)], it turns out the total, $E_{\mathcal{N}}^v$, and the scattered, $S_{\mathcal{N}}^v \triangleq (E_{\mathcal{N}}^v - E_{inc}^v)$, fields still comply with the *Data* and the *State* equations in the following form

$$E_{inc}^v(\mathbf{r}) = E_{\mathcal{N}}^v(\mathbf{r}) - \int_{\Omega} G_{\mathcal{B}}(\mathbf{r}, \mathbf{r}') \tau_{\mathcal{N}}(\mathbf{r}') E_{\mathcal{N}}^v(\mathbf{r}') d\mathbf{r}'; \quad \mathbf{r} \in \Omega; v = 1, \dots, V \quad (4)$$

$$S_{\mathcal{N}}^v(\mathbf{r}_m^v) = \int_{\Omega} G_{\mathcal{B}}(\mathbf{r}_m^v, \mathbf{r}') \tau_{\mathcal{N}}(\mathbf{r}') E_{\mathcal{N}}^v(\mathbf{r}') d\mathbf{r}'; \quad \mathbf{r}_m^v \in \Theta; v = 1, \dots, V; m = 1, \dots, M. \quad (5)$$

Accordingly, the contribution due to an unknown abnormal tissue can be isolated and made

explicit by defining a fictitious *Differential Scenario* as the difference between the actual and the reference ones [Fig. 1(b)]. In such a scenario, the v -th ($v = 1, \dots, V$) differential field, $D^v \triangleq (E^v - E_{\mathcal{N}}^v) = (S^v - S_{\mathcal{N}}^v)$, is computed by subtracting (4) from (2) to yield

$$D^v(\mathbf{r}) = \int_{\Omega} G_{\mathcal{N}}(\mathbf{r}, \mathbf{r}') \tau_{\Delta}(\mathbf{r}') E^v(\mathbf{r}') d\mathbf{r}'; \quad \mathbf{r} \in \Omega; v = 1, \dots, V \quad (6)$$

where $G_{\mathcal{N}}(\mathbf{r}, \mathbf{r}')$ is the inhomogeneous Green's function [8] of the reference distribution and τ_{Δ} is the differential contrast $\tau_{\Delta}(\mathbf{r}) \triangleq [\tau(\mathbf{r}) - \tau_{\mathcal{N}}(\mathbf{r})] = \frac{\tilde{\varepsilon}_A(\mathbf{r}) - \tilde{\varepsilon}_{\mathcal{N}}(\mathbf{r})}{\tilde{\varepsilon}_B}$, $\mathbf{r} \in \Psi$ [$\tau_{\Delta}(\mathbf{r}) \neq 0$ $\mathbf{r} \in \Psi$]. To numerically deal with the *ISP* at hand, the domain Ω is discretized into N square subdomains $\{\Omega_n \in \Omega; n = 1, \dots, N\}$ centered at $\{\mathbf{r}_n; n = 1, \dots, N\}$ so that the discretized form of equation (6) turns out to be

$$\underline{D}^{\Omega, v} = \underline{\underline{G}}_{\mathcal{N}}^{\Omega} \underline{J}_{\Delta}^v; \quad v = 1, \dots, V \quad (7)$$

where $\underline{D}^{\Omega, v} = \{D^v(\mathbf{r}_n); n = 1, \dots, N\}$, the entries of the vector $\underline{J}_{\Delta}^v = \{J_{\Delta}^v(\mathbf{r}_n); n = 1, \dots, N\}$ are the samples of the v -th ($v = 1, \dots, V$) differential equivalent current [$J_{\Delta}^v(\mathbf{r}_n) \triangleq \tau_{\Delta}(\mathbf{r}_n) E^v(\mathbf{r}_n)$], and $\underline{\underline{G}}_{\mathcal{N}}^{\Omega} \in \mathbb{C}^{N \times N}$ is the internal inhomogeneous Green's matrix given by (see Appendix A)

$$\underline{\underline{G}}_{\mathcal{N}}^{\Omega} = \left[\underline{\underline{\mathbb{I}}} - \underline{\underline{G}}_{\mathcal{B}}^{\Omega} \underline{\underline{\tau}}_{\mathcal{N}} \right]^{-1} \underline{\underline{G}}_{\mathcal{B}}^{\Omega}. \quad (8)$$

In (8), $\underline{\underline{\mathbb{I}}}$ is the $(N \times N)$ identity matrix, $\underline{\underline{\tau}}_{\mathcal{N}}$ is a square diagonal matrix which diagonal entries fill the vector $\underline{\tau}_{\mathcal{N}} = \{\tau_{\mathcal{N}}(\mathbf{r}_n); n = 1, \dots, N\}$, and $\underline{\underline{G}}_{\mathcal{B}}^{\Omega} \in \mathbb{C}^{N \times N}$ is the internal Green's matrix of the homogeneous background, which (n, s) -th ($n, s = 1, \dots, N$) element is given by $\underline{\underline{G}}_{\mathcal{B}}^{\Omega} \Big|_{n,s} \triangleq j \frac{\kappa_B^2}{4} \int_{\Omega_s} \mathcal{H}_0^{(2)}(\kappa_B \|\mathbf{r}_n - \mathbf{r}'\|) d\mathbf{r}'$, κ_B being the wavenumber, while $\mathcal{H}_0^{(2)}$ is the zero-th order Hankel function of the second kind and $\|\cdot\|$ indicates the ℓ_2 -norm.

On the other hand, the discretized data equation for the *Differential Scenario* reads as (see Appendix A)

$$\underline{D}^{\Theta, v} = \underline{\underline{G}}_{\mathcal{N}}^{\Theta, v} \underline{J}_{\Delta}^v; \quad v = 1, \dots, V \quad (9)$$

where the vector $\underline{D}^{\Theta, v} = \{D^v(\mathbf{r}_m^v); m = 1, \dots, M\}$ contains the samples of the v -th ($v = 1, \dots, V$) differential field computed in Θ and $\underline{\underline{G}}_{\mathcal{N}}^{\Theta, v} \in \mathbb{C}^{M \times N}$ is the v -th external inhomogeneous

Green's matrix

$$\underline{\underline{G}}_{\mathcal{N}}^{\Theta,v} = \underline{\underline{G}}_{\mathcal{B}}^{\Theta,v} \left[\underline{\underline{I}} + \underline{\underline{\tau}}_{\mathcal{N}} \underline{\underline{G}}_{\mathcal{N}}^{\Omega} \right], \quad (10)$$

$\underline{\underline{G}}_{\mathcal{B}}^{\Theta,v} \in \mathbb{C}^{M \times N}$ being the v -th ($v = 1, \dots, V$) external Green's matrix for the homogeneous background which (m, n) -th ($m = 1, \dots, M, n = 1, \dots, N$) element is given by $\underline{\underline{G}}_{\mathcal{B}}^{\Theta,v} \Big|_{m,n} \triangleq j \frac{\kappa_{\mathcal{B}}^2}{4} \int_{\Omega_n} \mathcal{H}_0^{(2)}(\kappa_{\mathcal{B}} \|\mathbf{r}_m^v - \mathbf{r}'\|) d\mathbf{r}'$. It should be highlighted that, since $\underline{\underline{G}}_{\mathcal{N}}^{\Omega}$ and $\underline{\underline{G}}_{\mathcal{N}}^{\Theta,v}$ only depend on $\Theta, \Omega, \underline{\underline{\tau}}_{\mathcal{N}}$, and $\tilde{\varepsilon}_{\mathcal{B}}$, they need to be computed only once by exploiting the available *a-priori* information on the *Reference Scenario*.

According to the previous formulation, the *MI* problem at hand can be rephrased as follows:

Breast Tumor ISP—Starting from the knowledge of the *reference* contrast, $\underline{\underline{\tau}}_{\mathcal{N}}$, the incident field within Ω , $\underline{\underline{E}}_{inc}^{\Omega,v} = \{E_{inc}^v(\mathbf{r}_n); n = 1, \dots, N\}$ ($v = 1, \dots, V$), and the differential field samples in Θ , $\underline{\underline{D}}^{\Theta,v}$ ($v = 1, \dots, V$), retrieve the unknown contrast distribution in Λ , $\underline{\underline{\tau}} = \{\tau(\mathbf{r}_n) = [\tau_{\mathcal{N}}(\mathbf{r}_n) + \tau_{\Delta}(\mathbf{r}_n)]; n = 1, \dots, N\}$ by determining the differential term $\underline{\underline{\tau}}_{\Delta} = \{\tau_{\Delta}(\mathbf{r}_n); n = 1, \dots, N\}$.

3 Physics-Driven AI Solution Approach

The “*Breast Tumor ISP*” is then reformulated into the following global optimization task

$$\underline{\underline{\alpha}}^{opt} = \arg \left\{ \min_{\underline{\underline{\alpha}}} [\Phi(\underline{\underline{\alpha}})] \right\} \quad (11)$$

where $\underline{\underline{\alpha}} = \{\alpha_k; k = 1, \dots, K\}$ is a set of properly-defined descriptors of the solution τ_{Δ} and $\Phi(\underline{\underline{\alpha}})$ is the differential data mismatch cost function

$$\Phi(\underline{\underline{\alpha}}) = \frac{\sum_{v=1}^V \|\underline{\underline{D}}^{\Theta,v}(\underline{\underline{\alpha}}) - \underline{\underline{D}}_{meas}^{\Theta,v}\|^2}{\sum_{v=1}^V \|\underline{\underline{D}}_{meas}^{\Theta,v}\|^2} \quad (12)$$

where $\underline{\underline{D}}^{\Theta,v}(\underline{\underline{\alpha}})$ and $\underline{\underline{D}}_{meas}^{\Theta,v}$ are the differential field associated to the solution τ_{Δ} defined by $\underline{\underline{\alpha}}$ and the one obtained from the measurements in Θ , respectively.

It is worth noticing that the efficient solution of (11) poses one paramount challenge to tackle, which directly comes from the high computational burden of an accurate full-wave evaluation

of (12). As a matter of fact, while global optimization solvers, such as those based on *EAs*, effectively explore the solution space without being trapped into false solutions (i.e., local minima) [35], they also require the iterated ($i = 1, \dots, I$, I being the number of iterations) evaluation of (12) for a population of P ($P \propto K$ [35]) agents (trial solutions). Therefore, it is mandatory to reduce the overall computational cost of the solution process to yield a solution as much as possible close to the actual one, $\underline{\alpha}^{act}$ within a reasonable (i.e., compatible with the clinical application) time frame.

Towards this end, a physics-driven *AI* solution strategy, inspired by the concepts/guidelines of the *SbD* paradigm [44] and leveraging the integration of a three-steps *LBE* strategy [40][41] with an *EA*-based global search engine [35], is adopted. More specifically, at each i -th ($i = 1, \dots, I$) iteration a *SM* of $\Phi(\underline{\alpha})$, $\widehat{\Phi}_i(\underline{\alpha})$, is exploited to make reliable-but-fast predictions of (12) starting from the information embedded in a training set \mathbb{O}_i of B_i previously-computed “examples”

$$\mathbb{O}_i = \{ [\underline{\alpha}_i^b, \Phi(\underline{\alpha}_i^b)] ; b = 1, \dots, B_i \}. \quad (13)$$

The three *logical* steps of the implemented *LBE* strategy are briefly summarized in the following and detailed in the next Sections:

1. *Physics-Driven Dimensionality Reduction* (Sect. 3.1) - Because of the “curse of dimensionality” [43] the number of training samples for an accurate prediction of (12) exponentially grows with the dimensionality K of the solution space. For such a reason, a traditional pixel-based expansion of the unknown dielectric profile in Ω is unfeasible since it would require a huge number of unknowns (i.e., $K = 2 \times N$) to code the permittivity and the conductivity in each discretization sub-domain $\{\Omega_n; n = 1, \dots, N\}$. Accordingly, the goal of this step is to seek a more convenient/efficient definition of $\underline{\alpha}$ (i.e., $K \ll 2N$), still guaranteeing a high flexibility in modeling the unknown target and allowing to embed *a-priori* information on the underlying physics;
2. *Adaptive Solution Space Sampling* (Sect. 3.2) - Once the low-cardinality set of descriptors $\underline{\alpha}$ has been defined (Step 1), the goal of this step is the proper selection of the minimum set of representative input-output pairs to build the *SM*. This task is performed by first

generating an initial ($i = 0$) training set $\mathbb{O}_0 = \{[\underline{\alpha}_0^b, \Phi(\underline{\alpha}_0^b)]; b = 1, \dots, B_0\}$ of B_0 samples uniformly spread over the K -dimensional search space. Successively, additional samples are progressively ($i = 1, \dots, I$) generated and added to the training set ($\mathbb{O}_0 \subseteq \dots \subseteq \mathbb{O}_i \subseteq \dots \subseteq \mathbb{O}_I$) to adaptively enhance the accuracy of the *SM* only in proximity of the actual solution/global optimum $\underline{\alpha}^{true}$. Such an adaptive sampling is performed by globally exploring the solution space with an *EA*-based strategy driven by the predictions and the associated degree of uncertainty outputted by the *SM*;

3. *Definition of the Learning Strategy* (Sect. 3.3) - This step is aimed at defining the most suitable *LBE* technique for exploiting the gathered information within \mathbb{O}_i to build the *SM* $\widehat{\Phi}_i(\underline{\alpha})$ ($i = 1, \dots, I$). Such a choice must take into account both the deterministic nature of (12) and the need to predict uncertainty measures supporting the *EA*-driven adaptive sampling (Step 2).

3.1 Physics-Driven Dimensionality Reduction

The definition of the minimum-cardinality set $\underline{\alpha}$ of K descriptors leverages the *prior* knowledge on the class of imaged targets as well as the underlying physics of the differential scattering formulation (Sect. 2). Since the *ISP* unknowns are expressed in terms of a physically-bounded difference with respect to a known reference *EM* scenario [Fig. 1(b)], the breast tumor is modeled as a relatively small region Ψ with homogeneous permittivity/conductivity values (i.e., $\varepsilon_{\mathcal{A}}(\mathbf{r}) = \varepsilon_{\Psi}$ and $\sigma_{\mathcal{A}}(\mathbf{r}) = \sigma_{\Psi}$, $\mathbf{r} \in \Psi$ [17][46]) and it is described with the vector $\underline{\alpha}$

$$\underline{\alpha} \triangleq \{\varepsilon_{\Psi}, \sigma_{\Psi}, x_{\Psi}, y_{\Psi}, \underline{d}\}. \quad (14)$$

In (14), x_{Ψ} and y_{Ψ} [$\mathbf{r}_{\Psi} = (x_{\Psi}, y_{\Psi}) \in \Lambda$] are the coordinates of the barycenter of Ψ , while $\underline{d} = \{d_c > 0; c = 1, \dots, C\}$ is a set of real values that univocally identifies its external contour $\partial\Psi$ (i.e., $\partial\Psi = \partial\Psi(\underline{d})$). More specifically, $\partial\Psi$ is defined as the union of C quadratic curves, $\partial\Psi = \bigcup_{c=1}^C \partial\Psi_c$, each c -th ($c = 1, \dots, C$) curve being expressed as the set of points complying with

$$\partial\Psi_c = \left\{ \forall \mathbf{r} \in \Lambda : \mathbf{r} = \mathbf{r}_c \times \left(\frac{1}{2} + l - l^2 \right) + \mathbf{r}_{c-1} \times \left(\frac{1}{2} - l + \frac{l^2}{2} \right) + \mathbf{r}_{c+1} \times \left(\frac{l^2}{2} \right); l \in [0, 1] \right\} \quad (15)$$

where

$$\mathbf{r}_c = \mathbf{r}_\Psi + d_c \times \boldsymbol{\beta}_c; \quad c = 1, \dots, C. \quad (16)$$

In (16) $\boldsymbol{\beta}_c = [\cos(\varphi_c), \sin(\varphi_c)]$ and $\varphi_c = 2\pi(c-1)/C$ ($c = 1, \dots, C$), while $\mathbf{r}_0 = \mathbf{r}_C$ and $\mathbf{r}_{C+1} = \mathbf{r}_1$. Accordingly, the dimensionality of the search space turns out to be significantly shrunk and equal to $K = (4 + C)$.

3.2 Adaptive Solution Space Sampling

The sampling of the K -dimensional solution space is aimed at three indivisible goals: (i) adaptively enhancing the accuracy of the *SM* within the *attraction basin* of the global optimum, (ii) effectively exploring the multi-minima landscape of the differential cost function (12), and (iii) minimizing the number of time-consuming full-wave evaluations. Such goals are achieved by integrating the *exploration* and the *exploitation* capabilities of both the *SM* and a multi-agent nature-inspired global optimizer. On the one hand, the *SM* exploits progressively-acquired information from the training samples to “understand” where new full-wave evaluations (i.e., new training samples) should be performed. This means identifying portions of the search space that should be further explored because of their higher probability of including $\underline{\alpha}^{true}$. On the other hand, the optimization engine exploits both the outputs of the *SM* and the acquired cognitive/social knowledge to smartly explore the search space by generating new trial guesses. Such an adaptive sampling starts from the generation of B_0 solutions $\{\underline{\alpha}_0^b; b = 1, \dots, B_0\}$, uniformly spread within the solution space by means of the Latin Hypercube Sampling (*LHS*) method [56].

The computation of the corresponding cost function values, $\{\Phi(\underline{\alpha}_0^b); b = 1, \dots, B_0\}$, is then performed after mapping each b -th ($b = 1, \dots, B_0$) sample into the corresponding dielectric map of Λ . With reference to a generic guess $\underline{\alpha}$, the following decoding rule is used

$$\tilde{\varepsilon}(\mathbf{r}_n | \underline{\alpha}) = \begin{cases} \varepsilon_0 \varepsilon_\Psi - j \frac{\sigma_\Psi}{\omega} & \text{if } \mathbf{r}_n \in \Psi(\underline{\alpha}) \\ \tilde{\varepsilon}_{\mathcal{N}}(\mathbf{r}_n) & \text{if } \mathbf{r}_n \in (\Lambda - \Psi(\underline{\alpha})) \end{cases}; \quad n = 1, \dots, N \quad (17)$$

where $\Psi(\underline{\alpha})$ is the tumor support described by $\underline{\alpha}$ (Sect. 3.1). Afterwards, the differential equivalent currents are determined as follows

$$\underline{J}_{\Delta}^v(\underline{\alpha}) = \underline{\tau}_{\Delta}(\underline{\alpha}) \left[\underline{\mathbb{I}} - \underline{G}_{\mathcal{B}}^{\Omega} \underline{\tau}(\underline{\alpha}) \right]^{-1} \underline{E}_{inc}^v; \quad v = 1, \dots, V \quad (18)$$

where $\underline{\tau}(\underline{\alpha})$ and $\underline{\tau}_{\Delta}(\underline{\alpha})$ are diagonal matrices which diagonal entries are given by $\underline{\tau}(\underline{\alpha}) = \{\tau(\mathbf{r}_n | \underline{\alpha}) = [\tilde{\varepsilon}(\mathbf{r}_n | \underline{\alpha}) / \tilde{\varepsilon}_{\mathcal{B}} - 1]; n = 1, \dots, N\}$ and $\underline{\tau}_{\Delta}(\underline{\alpha}) = \{\tau(\mathbf{r}_n | \underline{\alpha}) - \tau_{\mathcal{N}}(\mathbf{r}_n)\}; n = 1, \dots, N\}$, respectively. Finally, the differential field $\underline{D}^{\Theta, v}(\underline{\alpha})$ ($v = 1, \dots, V$) radiated by (18) is computed using (9) and then inputted to (12) to compute $\Phi(\underline{\alpha})$.

Such B_0 input-output examples are stored within \mathbb{O}_o and used to train an initial $SM \hat{\Phi}_0(\underline{\alpha})$. An iterative ($i = 1, \dots, I$) adaptive sampling is then repeated to explore the solution space by means of an *EA*-based strategy based on the Particle Swarm Optimization (*PSO*) operators [35]. More in detail, the following steps are performed:

1. *Initialization* ($i = 0$) - Randomly pick $P \leq B_0$ samples from \mathbb{O}_o to initialize a swarm of trial solutions $\Gamma_0 = \{\underline{\alpha}_0^p; p = 1, \dots, P\}$ and randomly set their velocities $\Upsilon_0 = \{\underline{v}_0^p; p = 1, \dots, P\}$. Initialize the personal best positions, $\underline{y}_0^p \leftarrow \underline{\alpha}_0^p$ ($p = 1, \dots, P$);

2. *Adaptive Sampling Loop* ($i = 1, \dots, I$)

- (a) *Population Prediction* - Use the i -th $SM \hat{\Phi}_i(\cdot)$ to predict the cost function associated to all agents of the population Γ_i , $\{\hat{\Phi}_i(\underline{\alpha}_i^p); p = 1, \dots, P\}$, and compute the corresponding uncertainties $\{\varsigma_i(\underline{\alpha}_i^p); p = 1, \dots, P\}$;

- (b) *Agent Selection* - Determine the best agent of the i -th population Γ_i as

$$\underline{\alpha}_i^* = \arg \left\{ \min_{\underline{\alpha} \in \Gamma_i} \left[\hat{\Phi}_i(\underline{\alpha}) - \varsigma_i(\underline{\alpha}) \right] \right\}; \quad (19)$$

- (c) *Training Set Updating* - If $\left[\hat{\Phi}_i(\underline{\alpha}_i^*) - \varsigma_i(\underline{\alpha}_i^*) \right] > \min_{\underline{\alpha} \in \mathbb{O}_i} \{\Phi(\underline{\alpha})\}$, then let $B_i \leftarrow B_{i-1}$, $\mathbb{O}_i \leftarrow \mathbb{O}_{i-1}$, $\hat{\Phi}_i(\cdot) \leftarrow \hat{\Phi}_{i-1}(\cdot)$ and jump to the next step. Otherwise, decode $\underline{\alpha}_i^*$ (17) and compute, through (18), the corresponding actual cost function value $\Phi(\underline{\alpha}_i^*)$. Then, let $B_i \leftarrow (B_{i-1} + 1)$, $\mathbb{O}_i \leftarrow \mathbb{O}_{i-1} \cup \{\underline{\alpha}_i^*, \Phi(\underline{\alpha}_i^*)\}$, and update the $SM \hat{\Phi}_i(\cdot)$ using \mathbb{O}_i ;

(d) *Personal Best Updating* - Update the personal best of each p -th ($p = 1, \dots, P$) agent

$$\underline{\vartheta}_i^p \leftarrow \mathcal{R} \{ \underline{\vartheta}_{i-1}^p, \underline{\alpha}_i^p \} \quad (20)$$

where $\mathcal{R} \{ \underline{\alpha}', \underline{\alpha}'' \}$ is a ranking operator selecting the “most promising” solution among the two inputs $\underline{\alpha}'$ and $\underline{\alpha}''$ by taking into account whether their cost function has been evaluated with the full-wave solver or predicted. More in detail, when both agents belong to the training set (i.e., $\{ \underline{\alpha}', \underline{\alpha}'' \} \in \mathbb{O}_i$) or not (i.e., $\{ \underline{\alpha}', \underline{\alpha}'' \} \notin \mathbb{O}_i$) the selection is based on their predicted cost function values along with the associated degree of reliability

$$\mathcal{R} \{ \underline{\alpha}', \underline{\alpha}'' \} \equiv \arg \left\{ \min_{\underline{\alpha} \in \{ \underline{\alpha}', \underline{\alpha}'' \}} \left[\widehat{\Phi}_i(\underline{\alpha}) - \varsigma_i(\underline{\alpha}) \right] \right\} \quad (21)$$

knowing that $\widehat{\Phi}_i(\underline{\alpha}) = \Phi(\underline{\alpha})$ and $\varsigma_i(\underline{\alpha}) = 0$ (i.e., exact knowledge and null uncertainty) if $\underline{\alpha}$ has been evaluated with the full-wave solver (i.e., $\underline{\alpha} \in \mathbb{O}_i$). Otherwise, when only one agent belongs to the set of full-wave simulated samples (e.g., $\underline{\alpha}' \notin \mathbb{O}_i$ and $\underline{\alpha}'' \in \mathbb{O}_i$), the predicted cost is “penalized” by the uncertainty, letting

$$\mathcal{R} \{ \underline{\alpha}', \underline{\alpha}'' \} \equiv \begin{cases} \underline{\alpha}' & \text{if } \left[\widehat{\Phi}_i(\underline{\alpha}') + \varsigma_i(\underline{\alpha}') \right] < \Phi(\underline{\alpha}'') \\ \underline{\alpha}'' & \text{otherwise;} \end{cases} \quad (22)$$

(e) *Global Best Updating* - Update the global best

$$\underline{\alpha}_i^{opt} \leftarrow \arg \left\{ \min_{\underline{\alpha} \in \Pi_i} \left[\widehat{\Phi}_i(\underline{\alpha}) + \varpi \times \varsigma_i(\underline{\alpha}) \right] \right\} \quad (23)$$

where the value of the constant ϖ depends on whether the global best at the $(i - 1)$ -th iteration was full-wave evaluated ($\underline{\alpha}_{i-1}^{opt} \in \mathbb{O}_{i-1} \Rightarrow \varpi = +1$) or not ($\underline{\alpha}_{i-1}^{opt} \notin \mathbb{O}_{i-1} \Rightarrow \varpi = -1$), while Π_i comprises both $\underline{\alpha}_{i-1}^{opt}$ and all personal best positions at the current iteration

$$\Pi_i \triangleq \underline{\alpha}_{i-1}^{opt} \cup \{ \underline{\vartheta}_i^p; p = 1, \dots, P \}; \quad (24)$$

(f) *Population Updating* - Apply the *PSO* operators [35] to update the agents velocities

$\Upsilon_{i+1} = \{\underline{v}_{i+1}^p; p = 1, \dots, P\}$ by exploiting the acquired cognitive (i.e., $\{\underline{v}_i^p; p = 1, \dots, P\}$) and social (i.e., $\underline{\alpha}_i^{opt}$) information, then update the p -th agent of the population

$$\underline{\alpha}_{i+1}^p \leftarrow (\underline{\alpha}_i^p + \underline{v}_{i+1}^p); p = 1, \dots, P. \quad (25)$$

Let $p \leftarrow (p + 1)$ and repeat from Step 2(a);

3. *Output Phase* - The global best at the last iteration ($i = I$) is selected as the result of the inversion ($\underline{\alpha}^{opt} \leftarrow \underline{\alpha}_{i=I}^{opt}$) and the reconstructed permittivity profile is computed through (17).

3.3 Definition of the Learning Strategy

At each i -th ($i = 1, \dots, I$) iteration of the adaptive sampling (Sect. 3.2), the training samples stored in \mathbb{O}_i are treated as they were observations of a normally distributed stochastic process. Accordingly, the correlation between any pair of samples $(\underline{\alpha}_i^a, \underline{\alpha}_i^b) \in \mathbb{O}_i$ is expressed in terms of Kriging basis functions [47],

$$w_i(\underline{\alpha}_i^a, \underline{\alpha}_i^b) \triangleq \exp\left(-\sum_{k=1}^K \theta_{i,k} |\alpha_{i,k}^a - \alpha_{i,k}^b|^{\nu_i}\right). \quad (26)$$

From (26), the $(B_i \times B_i)$ correlation matrix $\underline{\underline{W}}_i$ of \mathbb{O}_i is computed by setting its (a, b) -th entry ($a, b = 1, \dots, B_i$) to $\underline{\underline{W}}_i|_{a,b} = w_i(\underline{\alpha}_i^a, \underline{\alpha}_i^b)$. As for the real-valued hyper-parameters $\underline{\theta}_i = \{\theta_{i,k}; k = 1, \dots, K\}$ and ν_i in (26), they are found by maximizing the ‘‘joint likelihood’’ function [48]

$$\mathcal{L}(\underline{\theta}_i, \nu_i) = \frac{1}{(\sqrt{2\pi}\xi_i)^{B_i}} \exp\left[-\sum_{b=1}^{B_i} \frac{(\Phi(\underline{\alpha}_i^b) - \gamma_i)^2}{2\xi_i^2}\right], \quad (27)$$

where γ_i and ξ_i^2 are the maximum-likelihood estimates of the process average

$$\gamma_i = \frac{\sum_{a=1}^{B_i} \sum_{b=1}^{B_i} \underline{\underline{U}}_i|_{a,b} \Phi(\underline{\alpha}_i^b)}{\sum_{a=1}^{B_i} \sum_{b=1}^{B_i} \underline{\underline{U}}_i|_{a,b}}, \quad (28)$$

and its variance

$$\xi_i^2 = \frac{1}{B_i} \sum_{a=1}^{B_i} \sum_{b=1}^{B_i} (\Phi(\underline{\alpha}_i^a) - \gamma_i) \underline{U}_i \Big|_{a,b} (\Phi(\underline{\alpha}_i^b) - \gamma_i) \quad (29)$$

respectively being $\underline{U}_i \triangleq \underline{W}_i^{-1}$. Given the above formulation, the prediction of the cost function in correspondence with an arbitrary solution $\underline{\alpha}$ is given by [47]

$$\widehat{\Phi}_i(\underline{\alpha}) = \gamma_i + \sum_{a=1}^{B_i} \sum_{b=1}^{B_i} w_i(\underline{\alpha}, \underline{\alpha}_i^a) \underline{U}_i \Big|_{a,b} (\Phi(\underline{\alpha}_i^b) - \gamma_i), \quad (30)$$

while the associated prediction uncertainty is derived as

$$\varsigma_i(\underline{\alpha}) = 2\xi_i \sqrt{1 - \sum_{a=1}^{B_i} \sum_{b=1}^{B_i} w_i(\underline{\alpha}, \underline{\alpha}_i^a) \underline{U}_i \Big|_{a,b} w_i(\underline{\alpha}, \underline{\alpha}_i^b)}. \quad (31)$$

4 Numerical and Experimental Results

A set of representative benchmarks, concerned with both synthetic (Sects. 4.1-4.3) and experimental (Sect. 4.4) data, is presented to assess the performance of the proposed *SbD* inversion methodology in scenarios of increasing complexity/realism. Quantitatively, the reconstruction “quality” has been evaluated with the integral error metric

$$\Xi\{R\} \triangleq \frac{1}{N_R} \sum_{n=1}^{N_R} \frac{|\tau_\Delta(\mathbf{r}_n) - \tau_\Delta^{true}(\mathbf{r}_n)|}{|\tau_\Delta^{true}(\mathbf{r}_n) + 1|}, \quad (32)$$

where τ_Δ and τ_Δ^{true} are the retrieved and the actual differential contrasts, respectively, while $R \subseteq \Omega$ indicates the region comprising $N_R \leq N$ pixels where the computation has been performed (i.e., $\Xi_{tot} \triangleq \Xi\{R = \Omega\}$, $\Xi_{int} \triangleq \Xi\{R = \Psi\}$, and $\Xi_{ext} \triangleq \Xi\{R = (\Omega \setminus \Psi)\}$).

The numerical analysis has dealt with an imaging setup at $f = 1.3$ [GHz] comprising $V = 16$ line currents uniformly-distributed in a circle with radius $\rho_\Theta = 7.6$ [cm] from the barycenter of Ω . The synthetic data have been computed by solving the forward scattering equations discretized with a dense grid of cells $\lambda_{\min}/20$ -sided, λ_{\min} being the wavelength in the breast tissue with the highest permittivity. To avoid the “inverse crime” [8], a different (coarser) $\lambda_{\min}/10$ discretization has been adopted in the *ISP*. To emulate the measurement noise in a breast *MI*

setup, the total field has been blurred with an additive white Gaussian noise characterized by a signal-to-noise ratio (SNR) value.

4.1 Preliminary Analysis with “Ideal” Breast Phantom

The first illustrative example considers an “ideal” breast phantom immersed in a background matching medium of permittivity $\varepsilon_{\mathcal{B}} = 22.4$ and conductivity $\sigma_{\mathcal{B}} = 1.26$ [S/m] [17] with circular coronal section Λ and homogeneous characteristics [i.e., $\varepsilon_{\mathcal{N}}(\mathbf{r}) = \varepsilon_{\mathcal{N}} = 16.5$ and $\sigma_{\mathcal{N}}(\mathbf{r}) = \sigma_{\mathcal{N}} = 0.60$ [S/m] for $\mathbf{r} \in \Lambda$ [17] - Figs. 2(a)-2(b)⁽²⁾]. A circular tumor of radius $\rho_{\Psi} = 0.5$ [cm], permittivity $\varepsilon_{\Psi} = 59.3$, and conductivity $\sigma_{\Psi} = 1.54$ [S/m] [17] has been supposed to be present within the breast [Figs. 2(c)-2(d)]. For such a scenario, the performance of the proposed SbD approach have been compared to those of two standard inversion strategies formulated either in the DA or the EA frameworks by processing the numerically-computed data with $SNR = 100$ [dB] [17]. More specifically, a state-of-the-art CG exploiting pixel basis functions has been chosen as the DA strategy and it has been run for $I_{DA} = 400$ iterations to reach convergence [57]. Concerning the EA approach, a standard PSO algorithm [35] has been used to explore the solution space defined by $\underline{\alpha}$. The tumor shape has been modeled by setting $C = 4$ in (15), so that $K = 8$ unknowns. The number of agents and initial training samples have been set to $P = (2 \times K) = 16$ and $B_0 = (5 \times K) = 40$, respectively, according to the literature guidelines [37][44]. Finally, to guarantee a fair comparison between the SbD and the DA in terms of total computational cost, the number of both SbD and EA iterations has been set to match the time elapsed by one DA minimization (i.e., $\Delta t_{DA} \approx \Delta t_{SbD} \Rightarrow I = 200$).

The behavior of the cost function versus the iteration number is shown in Fig. 3(a). As it can be observed, the SbD remarkably minimizes the cost function until a value at the convergence ($i = I$) very close to that yielded by the EA [i.e., $|\Phi_I|_{SbD} - \Phi_I|_{EA} < 3 \times 10^{-5}$ - Fig. 3(a)]. The corresponding total reconstruction errors and execution times are given in Fig. 3(b) to point out that the SbD is able to provide almost the same solution “quality” of the EA [$\Xi_{tot}|_{SbD} = 2.01 \times 10^{-5}$ vs. $\Xi_{tot}|_{EA} = 1.46 \times 10^{-5}$ - Fig. 3(b)] with a significant reduction of the overall computational time [i.e., $\Delta t|_{SbD} = 7.38$ [min] vs. $\Delta t|_{EA} = 98.4$ [min], being $\Delta t|_{DA} = 7.40$

⁽²⁾For visualization purposes, only the color-scale permittivity/conductivity distributions within Λ are plotted.

[min]⁽³⁾ - Fig. 3(b)]. By defining the time saving of the *SbD* over the *EA* as

$$\eta = \frac{\Delta t|_{EA} - \Delta t|_{SbD}}{\Delta t|_{EA}} \approx 1 - \frac{B_I}{T}, \quad (33)$$

$T = (P \times I)$ being the number of full-wave evaluations performed by this latter, it turns out that $\eta = 93\%$. Such a speed-up enhancement is even more impressive when observing that almost identical reconstructions have been yielded by both methods as pictorially confirmed by the permittivity (left column) and conductivity (right column) maps in Fig. 4. Indeed, it turns out that the *SbD* inherits the *hill-climbing* features of a nature-inspired multi-agent exploration [35], escaping from the multiple local minima (false solutions) and properly guessing the position, the size, the shape, and the *EM* composition of the unknown abnormal tissue [Figs. 4(a)-4(b) vs. Figs. 2(c)-2(d)]. On the other hand, while being as fast as the *SbD*, the *DA* only roughly detects the presence of the tumor without accurate information on its size and composition [Figs. 4(e)-4(f)]. Such outcomes are also quantitatively confirmed by the value of the internal error [i.e., $\Xi_{int}|_{DA} = 6.18 \times 10^{-1}$ - Figs. 4(e)-4(f)], which is two orders in magnitude higher than that for the *SbD* [$\Xi_{int}|_{SbD} = 9.75 \times 10^{-3}$ - Figs. 4(a)-4(b)] and the *EA* [$\Xi_{int}|_{EA} = 7.08 \times 10^{-3}$ - Figs. 4(c)-4(d)]. Similar outcomes hold true for the external error because of the noticeable artifacts generated within Λ , as well (i.e., $\Xi_{ext}|_{DA} = 1.24 \times 10^{-2}$ vs. $\Xi_{ext}|_{SbD} = \Xi_{ext}|_{EA} = 0.0$).

4.2 Analysis with Segmented Breast Phantom

While the “ideal” phantom of Sect. 4.1 is an over-simplification of the actual breast structure, which generally includes several tissues with inhomogeneous *EM* characteristics, it was an useful benchmark to test the features of the *SbD* approach. However, let us consider a more faithful/realistic representation of the breast anatomy. More specifically, the numerical phantoms from the *UWCEM* repository, an open-access dataset of *MRI*-derived breast models with realistic geometrical and *EM* features [45], have been used. Such a biomedical database includes phantoms belonging to all four categories of breast composition identified by the American College of Radiology [49] [i.e., (a) “fatty”, (b) “scattered”, (c) “heterogeneously dense” (*HD*), and

⁽³⁾These CPU times refer to non-optimized FORTRAN codes on a standard laptop with 16 [GB] of RAM memory and an Intel(R) Core(TM) i5-8250U CPU @ 1.60 [GHz].

(*d*) “extremely dense” (*XD*) that correspond to increasing concentrations of high-permittivity tissues.

Dealing with piece-wise (i.e., segmented) homogeneous breast models, a phantom belonging to the *XD* category (*UWCEM ID* 012304, coronal slice Λ at $z_\Lambda = 6.65$ [cm] [45]) has been considered first. Following the guidelines in [17], each cell of the reference breast has been binary classified into two types of tissue, namely “adipose” and “fibroglandular”, which dielectric properties are reported in Tab. I. Moreover, the skin layer has been approximated as “adipose” tissue [17] since the breast has been assumed to be immersed in a bath of matching medium ($\epsilon_B = 22.4$, $\sigma_B = 1.26$ [S/m] [17] - Tab. I) and the thickness of such a layer is generally electrically negligible ($t_{skin} = 1.5$ [mm] $\approx 5\%$ of λ_{min} [17]). As for the tumor, it has been modeled as an ellipse which shape and size match one of the realistic phantoms described in [50] [Figs. 5(a)-5(b)]. The *SbD* reconstruction in Figs. 5(c)-5(d) positively compares with the actual configuration [Figs. 5(a)-5(b)] even though the value of the total error (i.e., $\Xi_{tot} = 3.21 \times 10^{-3}$) increases with respect to the ideal case in Sect. 4.1 because of the increased complexity of the scenario at hand.

To investigate on the reliability and the robustness of the *SbD* in case of higher levels of noise, an analysis has been performed by varying the *SNR* from $SNR = 100$ [dB] down to $SNR = 10$ [dB]. The inversion results are summarized in Fig. 6 in terms of total [Fig. 6(a)], internal [Fig. 6(b)], and external [Fig. 6(c)] errors. As it can be observed, the *SbD* accuracy is always comparable to that of the *EA* and remarkably higher than the *DA* whatever the blurring of the processed data. As a representative example, Figure 7 shows the breast profiles reconstructed by the three algorithms when $SNR = 20$ [dB]. Despite the harsh noise conditions, the *SbD* map is still highly similar to the actual one [$\Xi_{tot}|_{SbD} = 4.38 \times 10^{-3}$ - Figs. 7(a)-7(b) vs. Figs. 5(a)-5(b)], with the same reconstruction accuracy of the *EA* inversion [$\Xi_{tot}|_{EA} = 3.65 \times 10^{-3}$ - Figs. 7(c)-7(d)] and visibly better than the *DA* one [$\Xi_{tot}|_{DA} = 9.22 \times 10^{-2}$ - Figs. 7(e)-7(f)]. Additionally, the *SbD* is always significantly faster than the *EA* with a time saving of $\eta = 93\%$ because of the reduction of the calls to the full-wave solver thanks to the exploitation of the *SM* [Fig. 6(d)].

The *SbD* accuracy has then been assessed by considering breasts with different densities, as

well. Towards this end, three additional *UWCEM* phantoms have been selected either belonging to the fatty, the scattered, and the *HD* categories (Tab. I). Figure 8 compares the *SbD* errors for each considered class, while Figure 9 shows the corresponding reconstructions. It turns out that the *SbD* performance are quite similar in all benchmark scenarios, even though the total error slightly increases when the breast density changes from the *XD* to the “fatty” one (i.e., $\Xi_{tot}|_{Fatty} / \Xi_{tot}|_{XD} \approx 2.0$ - Fig. 8). This is not a surprise, since a reduced breast density translates into lower values of the reference permittivity, $\varepsilon_{\mathcal{N}}(\mathbf{r})$, and conductivity, $\sigma_{\mathcal{N}}(\mathbf{r})$, distributions (Tab. I), thus a higher differential contrast, $\tau_{\Delta}(\mathbf{r})$, have to be imaged, which result in a higher non-linearity of the corresponding *ISP*. Nevertheless, the *SbD* inversion always provides a precise indication of both the tumor location and its shape, as pictorially pointed out in Fig. 9.

The proposed method has been also tested against the variations of the *EM* properties of the tumor. Towards this aim, the complex permittivity of the abnormal tissue has been varied according to the following rule

$$\tilde{\varepsilon}_{\Psi}(\delta) = (1 + \delta) \tilde{\varepsilon}_{\Psi}^{nom} \quad (34)$$

where $\tilde{\varepsilon}_{\Psi}^{nom}$ is the nominal tumor permittivity ($\tilde{\varepsilon}_{\Psi}^{nom} = 59.3\varepsilon_0 - j\frac{1.54}{2\pi f}$) while δ has been set within the range $-10\% \leq \delta \leq 10\%$ according to the observed variability in *EM* properties of *ex-vivo* breast cancer biological samples [51]. The plots of the error metrics versus the δ value are shown in Fig. 10. Such results verify the robustness and general effectiveness of the proposed inversion method. As it can be observed, the error values are almost constant and the retrieved images of Λ turn out to be accurate even in the most challenging case with the highest differential contrast [i.e., $\delta = +10\% \rightarrow \Xi_{tot}|_{\delta=+10\%} = 3.1 \times 10^{-3}$ - Fig. 11(d) vs. Fig. 11(b) and Fig. 11(h) vs. Fig. 11(f)].

4.3 Analysis with Fully Inhomogeneous Breast Phantom

In this section, the most complex case where the complex permittivity values are available for each pixel belonging to Λ [52] is taken into account. More specifically, a “full” breast model has been derived from the *UWCEM* database [*ID* 012204 - Figs. 12(a)-12(b)] to provide a more detailed representation of the internal breast structure than its segmented [Figs. 12(c)-12(d)]

and constant [Figs. 12(e)-12(f)] versions that have been obtained by averaging the permittivity of each tissue type or of the entire coronal slice, respectively. Regardless of the more complex reference scenario, the *SbD* faithfully guesses the abnormal tissue distribution [Figs. 13(c)-13(d) vs. Figs. 13(a)-13(b)] by keeping the same features shown in the previous test cases when compared to other *SoA* inversion techniques (Tab. II).

It is now worth noticing that the benchmarks discussed so far considered the full *prior* (*FP*) knowledge of the reference breast tissues distribution. However, only partial/simplified information on the patient's breast is generally *a-priori* available in practical biomedical imaging. Accordingly, the following analysis investigates the *SbD* performance with *prior* knowledge on the reference scenario of diminishing accuracy. By considering the same actual scenario of Figs. 13(a)-13(b) for the forward scattering data computation, the segmented *prior* [*SP* - Figs. 12(c)-12(d)] or the constant one [*CP* - Figs. 12(e)-12(f)] have been inputted to the *SbD* to perform the inversion. The reconstructions starting from a *SP* [Figs. 13(e)-13(f)] are slightly less accurate than those for the *FP* case, but they still are of good quality in terms of estimated size and complex permittivity of the tumor. As a matter of fact, the total error increases by 35% between the *SP* and *FP* cases [Figs. 13(e)-13(f) vs. Figs. 13(c)-13(d) - Tab. III].

In the most challenging case of an over-simplified *CP*, totally neglecting the internal structure of the actual breast tissues [Figs. 12(e)-12(f) vs. Figs. 12(a)-12(b)], there is still a proper detection and localization of the tumor, even though its size is over-estimated as quantitatively pointed out by the increase of the external error [$\Xi_{ext}|_{CP} = 3.52 \times 10^{-2}$ vs. $\Xi_{ext}|_{FP} = 1.72 \times 10^{-3}$ - Figs. 13(g)-13(h) vs. 13(c)-13(d) and Tab. III].

4.4 Analysis with Experimental Phantoms

The final assessment is concerned with real scattering data and the inversion of experimental measurements at $f = 2$ [GHz] from the University of Manitoba Breast Microwave Imaging Dataset (*UM-BMID*, 3rd generation [25][58]). The *UM-BMID* contains data from various 3D-printed breast phantoms in air ($\epsilon_B = 1$, $\sigma_B = 0$ [S/m]). The measurements have been collected with a bi-static setup consisting of two *LB-20200-SF* horn antennas [53] located at $\rho_\Theta = 18$ [cm] from the center of the investigation domain and 72 [deg] apart from each other. A multi-

view/illumination imaging system has been implemented by rotating the system in $V = 72$ different angular positions with 5 [deg] steps [25][58].

The first experiment is related to a tumor of circular section and radius $\rho_{\Psi}^{true} = 1.5$ [cm] embedded within a breast phantom of “fatty” density. The coronal section of the actual permittivity and conductivity distributions are shown in Figs. 14(a)-14(b). Once again, the *SbD* reconstruction [Figs. 14(c)-14(d)] well resembles the one outputted by the *EA* [Figs. 14(e)-14(f)] by yielding, unlike the *DA* [Figs. 14(g)-14(h)], accurate qualitative and quantitative information on the tumor. There is only a slight over/under estimation of the relative permittivity/conductivity of the anomalous tissue as also indicated by the corresponding error indexes (e.g., $\Xi_{int}|_{\rho_{\Psi}^{true}=1.5}^{EA}$ [cm] / $\Xi_{int}|_{\rho_{\Psi}^{true}=1.5}^{SbD}$ [cm] ≈ 1.1 and $\Xi_{int}|_{\rho_{\Psi}^{true}=1.5}^{DA}$ [cm] / $\Xi_{int}|_{\rho_{\Psi}^{true}=1.5}^{SbD}$ [cm] ≈ 2.8 - Tab. IV), the speed-up still being $\Delta t|_{EA} / \Delta t|_{SbD} \approx 14.5$ times with respect to the standard global optimization ($\rightarrow \eta = 93\%$ - Tab. IV).

To give some insights towards the clinical exploitation of the proposed imaging approach, let us analyze the spatial resolution of the tumor localization by evaluating the following key-performance indicator [25]

$$\zeta \triangleq \|\mathbf{r}_{\Psi} - \mathbf{r}_{\Psi}^{true}\| \quad (35)$$

$\mathbf{r}_{\Psi}/\mathbf{r}_{\Psi}^{true}$ being the retrieved/actual tumor barycenter, respectively. Moreover, let the tumor detection be successful (i.e., marked as “Yes” in Tab. V) when the value of ζ complies with

$$\zeta \leq (\rho_{\Psi}^{true} + \chi), \quad (36)$$

$\chi = 0.5$ [cm] being the measurement uncertainty in the position of the tumor within the experimental breast phantom [25].

For comparison purposes, Table V resumes the results from the inversions with the *SbD*, the *EA*, and the *DA* along with those of other competitive alternatives in the available literature (i.e., the *DAS*, *DMAS*, and *ORR* methods [25]). Although all approaches positively operate since (36) is always verified, the *SbD* and the *EA* provide the lowest errors (i.e., $\zeta|_{SbD} = 0.48$ [cm] $\simeq \zeta|_{EA} = 0.45$ [cm] - Tab. V).

The last scenario is very challenging since it considers the diagnosis of a significantly smaller

tumor [i.e., $\rho_{\Psi}^{true} = 0.75$ [cm] - Figs. 15(a)-15(b)]. Such a benchmark is of particular biomedical interest since a 7-year survival rate of 84% is expected for patients that are diagnosed in the early stages of breast cancer (i.e., $\rho_{\Psi}^{true} \leq 0.75$ [cm] [54]), but unfortunately tumors of such a small size are quite hard to detect because of their weak scattering signature [55]. The *SbD* reconstruction in Figs. 15(c)-15(d) allows one to suitably estimate both the tumor size and shape, but there are some inaccuracies in its localization and composition that are quantified by an increment of both Ξ_{int} and ζ with respect to the previous test case (i.e., $\Xi_{ext}|_{\rho_{\Psi}^{true}=0.75}$ [cm] / $\Xi_{ext}|_{\rho_{\Psi}^{true}=1.5}$ [cm] ≈ 1.6 and $\zeta|_{\rho_{\Psi}^{true}=0.75}$ [cm] / $\zeta|_{\rho_{\Psi}^{true}=1.5}$ [cm] ≈ 2.1 - Figs. 15(c)-15(d) vs. Figs. 14(c)-14(d) and Tabs. IV-V). On the other hand, only the *SbD* and the *EA* prove to be able to detect the unknown pathology according to (36) (Tab. V).

5 Conclusions

A new physics-driven *AI* approach for a reliable and time-effective *MI* of breast tumors has been presented. Based on a proper differential formulation of the biomedical *ISP* at hand to enable the exploitation of *a-priori* physical knowledge on the imaged domain as well as a compact yet flexible description of the unknown pathology, an *AI*-based strategy [40] inspired by the concepts and guidelines of the *SbD* paradigm [37][44] has been proposed by reformulating the inversion of differential scattering data as a global optimization problem efficiently and reliably solved thanks to an adaptively-refined *SM* of the cost function.

The numerical and experimental assessments (Sect. 4) have shown that the proposed *MI* method

- is able to retrieve faithful guesses of the breast with a degree of accuracy comparable to a traditional global search based on *EAs*, but at a remarkably reduced computational cost being fast as a *DA*-based local search;
- exhibits a remarkable robustness against the noise blurring the differential scattering data;
- reliably retrieves tumors embedded within breasts of different densities, showing almost independent performance on the level of contrast between abnormal and normal tissues;

- properly performs also in case of an imperfect/approximated knowledge of the reference (healthy) breast tissues and internal structure;
- shows promising performance also when applied to real experimental data by overcoming competitive approaches even more when imaging small (i.e., early stages) tumoral pathologies.

Future works, beyond the scope of this article, will be aimed at extending the proposed imaging method to fully 3-D geometries as well as to investigate proper customizations to other biomedical applications of undoubted interest (e.g., brain stroke imaging).

Appendix A

To derive the expression for the inhomogeneous internal Green's matrix $\underline{\underline{G}}_{\mathcal{N}}^{\Omega}$, equation (4) is first subtracted from (2). Then, by exploiting the definition of $D^v(\mathbf{r})$ and $\tau_{\Delta}(\mathbf{r})$, one obtains

$$D^v(\mathbf{r}) = \int_{\Omega} G_{\mathcal{B}}(\mathbf{r}, \mathbf{r}') [\tau_{\Delta}(\mathbf{r}') E^v(\mathbf{r}') + \tau_{\mathcal{N}}(\mathbf{r}') D^v(\mathbf{r}')] d\mathbf{r}' \quad (37)$$

$$\mathbf{r} \in \Omega; v = 1, \dots, V$$

that in matrix notation becomes

$$\underline{\underline{D}}^{\Omega, v} = \underline{\underline{G}}_{\mathcal{B}}^{\Omega} \underline{\underline{J}}_{\Delta}^v + \underline{\underline{G}}_{\mathcal{B}}^{\Omega} \underline{\underline{\tau}}_{\mathcal{N}} \underline{\underline{D}}^{\Omega, v}; \quad v = 1, \dots, V. \quad (38)$$

By simple algebraic manipulations on (38), it turns out that

$$\underline{\underline{D}}^{\Omega, v} = \left\{ \left[\underline{\underline{\mathbb{I}}} - \underline{\underline{G}}_{\mathcal{B}}^{\Omega} \underline{\underline{\tau}}_{\mathcal{N}} \right]^{-1} \underline{\underline{G}}_{\mathcal{B}}^{\Omega} \right\} \underline{\underline{J}}_{\Delta}^v; \quad v = 1, \dots, V \quad (39)$$

so that it is possible to derive the definition of $\underline{\underline{G}}_{\mathcal{N}}^{\Omega}$ in (8).

Similarly, equation (5) is subtracted from (3) to yield

$$D^v(\mathbf{r}_m^v) = \int_{\Omega} G_{\mathcal{B}}(\mathbf{r}_m^v, \mathbf{r}') [\tau_{\Delta}(\mathbf{r}') E^v(\mathbf{r}') + \tau_{\mathcal{N}}(\mathbf{r}') D^v(\mathbf{r}')] d\mathbf{r}' \quad (40)$$

$$\mathbf{r}_m^v \in \Theta; v = 1, \dots, V; m = 1, \dots, M$$

that after discretization becomes

$$\underline{D}^{\Theta,v} = \underline{G}_{\mathcal{B}}^{\Theta,v} \left[\underline{J}_{\Delta}^v + \underline{\tau}_{\mathcal{N}} \underline{D}^{\Omega,v} \right]; \quad v = 1, \dots, V. \quad (41)$$

Finally, by substituting $\underline{D}^{\Omega,v}$ with (7) in (41), we obtain

$$\underline{D}^{\Theta,v} = \left\{ \underline{G}_{\mathcal{B}}^{\Theta,v} \left[\underline{\mathbb{I}} + \underline{\tau}_{\mathcal{N}} \underline{G}_{\mathcal{N}}^{\Omega} \right] \right\} \underline{J}_{\Delta}^v; \quad v = 1, \dots, V \quad (42)$$

to deduce the definition of the inhomogeneous external Green's matrix $\underline{G}_{\mathcal{N}}^{\Theta}$ in (10).

Acknowledgments

This work benefited from the networking activities carried out within the Project ‘‘ICSC National Centre for HPC, Big Data and Quantum Computing (CN HPC)’’ funded by the European Union - NextGenerationEU within the PNRR Program (CUP: E63C22000970007), the Project ‘‘AURORA - Smart Materials for Ubiquitous Energy Harvesting, Storage, and Delivery in Next Generation Sustainable Environments’’ funded by the Italian Ministry for Universities and Research within the PRIN-PNRR 2022 Program (CUP: E53D23014760001), the Project DICAM-EXC (Grant L232/2016) funded by the Italian Ministry of Education, Universities and Research (MUR) within the ‘‘Departments of Excellence 2023-2027’’ Program (CUP: E63C22003880001), and the Project ‘‘SPEED’’ (Grant No. 6721001) funded by National Science Foundation of China under the Chang-Jiang Visiting Professorship Program. Views and opinions expressed are however those of the author(s) only and do not necessarily reflect those of the European Union or the European Research Council. Neither the European Union nor the granting authority can be held responsible for them. A. Massa wishes to thank E. Vico for her never-ending inspiration, support, guidance, and help.

References

- [1] World Health Organization, “Breast cancer”. Accessed: Nov. 4, 2022. [Online]. Available: <https://www.who.int/news-room/fact-sheets/detail/breast-cancer>
- [2] L. Tabar, P. B. Dean, T. H. Chen, A. M. Yen, S. L. Chen, J. C. Fann, S. Y. Chiu, M. M. Ku, W. Y. Wu, C. Hsu, Y. Chen, K. Beckmann, R. A. Smith, and S. W. Duffy, “The incidence of fatal breast cancer measures the increased effectiveness of therapy in women participating in mammography screening,” *Cancer*, vol. 125, no. 4, pp. 515-523, Feb. 2019.
- [3] N. Nikolova, “Microwave imaging for breast cancer,” *IEEE Microw. Mag.*, vol. 12, no. 7, pp. 78-94, Dec. 2011.
- [4] A. Mirbeik-Sabzevari and N. Tavassolian, “Tumor detection using millimeter-wave technology: Differentiating between benign lesions and cancer tissues,” *IEEE Microw. Mag.*, vol. 20, no. 8, pp. 30-43, Aug. 2019.
- [5] M. Bassi, M. Caruso, M. S. Khan, A. Bevilacqua, A.-D. Capobianco, and A. Neviani, “An integrated microwave imaging radar with planar antennas for breast cancer detection,” *IEEE Trans. Microw. Theory Techn.*, vol. 61, no. 5, pp. 2108-2118, May 2013.
- [6] E. Porter, H. Bahrami, A. Santorelli, B. Gosselin, L. A. Rusch, and M. Popovic, “A wearable microwave antenna array for time-domain breast tumor screening,” *IEEE Trans. Med. Imaging*, vol. 35, no. 6, pp. 1501-1509, Jun. 2016.
- [7] D. O’Loughlin, M. O’Halloran, B. M. Moloney, M. Glavin, E. Jones, and M. A. Elahi, “Microwave breast imaging: Clinical advances and remaining challenges,” *IEEE Trans. Biomed. Eng.*, vol. 65, no. 11, pp. 2580-2590, Nov. 2018.
- [8] X. Chen, *Computational Methods for Electromagnetic Inverse Scattering*. Hoboken, NJ, USA: Wiley, 2018.
- [9] S. Caorsi, A. Massa, M. Pastorino, and M. Donelli, “Improved microwave imaging procedure for nondestructive evaluations of two-dimensional structures,” *IEEE Trans. Antennas Propag.*, vol. 52, no. 6, pp. 1386-1397, Jun. 2004.

- [10] K. Xu, Y. Zhong, X. Chen, and D. Lesselier, "A fast integral equation-based method for solving electromagnetic inverse scattering problems with inhomogeneous background," *IEEE Trans. Antennas Propag.*, vol. 66, no. 8, pp. 4228-4239, Aug. 2018.
- [11] D. Kurrant and E. Fear, "Defining regions of interest for microwave imaging using near-field reflection data," *IEEE Trans. Microw. Theory Techn.*, vol. 61, no. 5, pp. 2137-2145, May 2013.
- [12] T. J. Colgan, S. C. Hagness, and B. D. Van Veen, "A 3-D level set method for microwave breast imaging," *IEEE Trans. Biomed. Eng.*, vol. 62, no. 10, pp. 2526-2534, Oct. 2015.
- [13] N. Abdollahi, I. Jeffrey, and J. LoVetri, "Improved tumor detection via quantitative microwave breast imaging using eigenfunction-based prior," *IEEE Trans. Comput. Imaging*, vol. 6, pp. 1194-1202, Jul. 2020.
- [14] E. Porter, M. Coates, and M. Popovic, "An early clinical study of time-domain microwave radar for breast health monitoring," *IEEE Trans. Biomed. Eng.*, vol. 63, no. 3, pp. 530-539, Mar. 2016.
- [15] K. Smith, J. Bourqui, D. Garrett, S. Zarnke, M. Owjimehr, D. Deutscher, T. Fung, and E. Fear, "Microwave imaging of the breast: Consistency of measurements over time," *IEEE J. Electromagn. RF Microw. Med. Biol.*, vol. 6, no. 1, pp. 61-67, Mar. 2022.
- [16] A. Gubern-Merida, M. Kallenberg, R. M. Mann, R. Marti, and N. Karssemeijer, "Breast segmentation and density estimation in breast MRI: A fully automatic framework," *IEEE J. Biomed. Health Inform.*, vol. 19, no. 1, pp. 349-357, Jan. 2015.
- [17] A. H. Golnabi, P. M. Meaney, S. D. Geimer, and K. D. Paulsen, "3-D microwave tomography using the soft prior regularization technique: Evaluation in anatomically realistic MRI-derived numerical breast phantoms," *IEEE Trans. Biomed. Eng.*, vol. 66, no. 9, pp. 2566-2575, Sep. 2019.
- [18] N. Abdollahi, D. Kurrant, P. Mojabi, M. Omer, E. Fear, and J. LoVetri, "Incorporation of ultrasonic prior information for improving quantitative microwave imaging of breast," *IEEE J. Multiscale Multiphys. Comput. Tech.*, vol. 4, pp. 98-110, Mar. 2019.

- [19] P. Mojabi and J. LoVetri, "Experimental evaluation of composite tissue-type ultrasound and microwave imaging," *IEEE J. Multiscale Multiphys. Comput. Tech.*, vol. 4, pp. 119-132, Mar. 2019.
- [20] Y. Qin, T. Rodet, M. Lambert, and D. Lesselier, "Microwave breast imaging with prior ultrasound information," *IEEE Open J. Antennas Propag.*, vol. 1, pp. 472-482, Aug. 2020.
- [21] H. B. Lim, N. T. T. Nhung, E.-P. Li, and N. D. Thang, "Confocal microwave imaging for breast cancer detection: Delay-multiply-and-sum image reconstruction algorithm," *IEEE Trans. Biomed. Eng.*, vol. 55, no. 6, pp. 1697-1704, June 2008.
- [22] E. C. Fear, J. Bourqui, C. Curtis, D. Mew, B. Docktor, and C. Romano, "Microwave breast imaging with a monostatic radar-based system: A study of application to patients," *IEEE Trans. Microw. Theory Techn.*, vol. 61, no. 5, pp. 2119-2128, May 2013.
- [23] T. Gholipur, M. Nakhkash, and M. Zoofaghari, "A linear synthetic focusing method for microwave imaging of 2-D objects," *IEEE Trans. Microw. Theory Techn.*, pp. 5042-5050, Nov. 2018.
- [24] S. Mukherjee, L. Udpa, S. Udpa, E. J. Rothwell, and Y. Deng, "A time reversal-based microwave imaging system for detection of breast tumors," *IEEE Trans. Microw. Theory Techn.*, vol. 67, no. 5, pp. 2062-2075, May 2019.
- [25] T. Reimer and S. Pistorius, "An optimization-based approach to radar image reconstruction in breast microwave sensing," *Sensors*, vol. 21, no. 24, pp. 8172, Dec. 2021.
- [26] M. R. Casu, M. Vacca, J. A. Tobon, A. Pulimeno, I. Sarwar, R. Solimene, and F. Vipiana, "A COTS-based microwave imaging system for breast-cancer detection," *IEEE Trans. Biomed. Circuits Syst.*, vol. 11, no. 4, pp. 804-814, Aug. 2017.
- [27] S. P. Poplack, T. D. Tosteson, W. A. Wells, B. W. Pogue, P. M. Meaney, A. Hartov, C. A. Kogel, S. K. Soho, J. J. Gibson, and K. D. Paulsen, "Electromagnetic breast imaging: Results of a pilot study in women with abnormal mammograms," *Radiology*, vol. 243, no. 2, pp. 350-359, May 2007.

- [28] P. M. Meaney, P. A. Kaufman, L. S. Muffly, M. Click, S. P. Poplack, W. A. Wells, G. N. Schwartz, R. M. di Florio-Alexander, T. D. Tosteson, Z. Li, S. D. Geimer, M. W. Fanning, T. Zhou, N. R. Epstein, and K. D. Paulsen, "Microwave imaging for neoadjuvant chemotherapy monitoring: Initial clinical experience," *Breast Cancer Research*, vol. 15, no. 2, Apr. 2013.
- [29] Z. Miao and P. Kosmas, "Multiple-frequency BBIM-TwIST algorithm for microwave breast imaging," *IEEE Trans. Antennas Propag.*, vol. 65, no. 5, pp. 2507-2516, May 2017.
- [30] L. M. Neira, B. D. Van Veen, and S. C. Hagness, "High-resolution microwave breast imaging using a 3-D inverse scattering algorithm with a variable-strength spatial prior constraint," *IEEE Trans. Antennas Propag.*, vol. 65, no. 11, pp. 6002-6014, Nov. 2017.
- [31] D. Tajik, R. Kazemivala, and N. K. Nikolova, "Real-time imaging with simultaneous use of Born and Rytov approximations in quantitative microwave holography," *IEEE Trans. Microw. Theory Techn.*, vol. 70, no. 3, pp. 1896-1909, Mar. 2022.
- [32] F. Gao, B. D. Van Veen, and S. C. Hagness, "Sensitivity of the distorted Born iterative method to the initial guess in microwave breast imaging," *IEEE Trans. Antennas Propag.*, vol. 63, no. 8, pp. 3540-3547, Aug. 2015.
- [33] S. Hosseinzadegan, A. Fhager, M. Persson, S. D. Geimer, and P. M. Meaney, "Discrete dipole approximation-based microwave tomography for fast breast cancer imaging," *IEEE Trans. Microw. Theory Techn.*, vol. 69, no. 5, pp. 2741-2752, May 2021.
- [34] Q. H. Liu, Z. Q. Zhang, T. T. Wang, J. A. Bryan, G. A. Ybarra, L. W. Nolte, and W. T. Joineset, "Active microwave imaging. I. 2-D forward and inverse scattering methods," *IEEE Trans. Microw. Theory Techn.*, vol. 50, no. 1, pp. 123-133, Jan. 2002.
- [35] P. Rocca, M. Benedetti, M. Donelli, D. Franceschini, and A. Massa, "Evolutionary optimization as applied to inverse scattering problems," *Inverse Probl.*, vol. 25, no. 12, 123003, Dec. 2009.
- [36] P. Rocca, G. Oliveri, and A. Massa, "Differential evolution as applied to electromagnetics," *IEEE Antennas Propag. Mag.*, vol. 53, no. 1, pp. 38-49, Feb. 2011

- [37] M. Salucci, L. Poli, P. Rocca, and A. Massa, "Learned global optimization for inverse scattering problems: Matching global search with computational efficiency," *IEEE Trans. Antennas Propag.*, vol. 70, no. 8, pp. 6240-6255, Aug. 2022.
- [38] M. Pastorino, "Stochastic optimization methods applied to microwave imaging: A review," *IEEE Trans. Antennas Propag.*, vol. 55, no. 3, pp. 538-548, Mar. 2007.
- [39] S. Goudos, *Emerging Evolutionary Algorithms for Antennas and Wireless Communications*. SciTech/IET, 2021 (ISBN-13: 978-1-78561-552-8).
- [40] M. Salucci, M. Arrebola, T. Shan, and M. Li, "Artificial intelligence: New frontiers in real-time inverse scattering and electromagnetic imaging," *IEEE Trans. Antennas Propag.*, vol. 70, no. 8, pp. 6349-6364, Aug. 2022
- [41] A. Massa, G. Oliveri, M. Salucci, N. Anselmi, and P. Rocca, "Learning-by-examples techniques as applied to electromagnetics," *J. Electromagn. Waves Appl.*, vol. 32, no. 4, pp. 516-541, 2018.
- [42] Y. Zhou, Y. Zhong, Z. Wei, T. Yin, and X. Chen, "An improved deep learning scheme for solving 2-D and 3-D inverse scattering problems," *IEEE Trans. Antennas Propag.*, vol. 69, no. 5, pp. 2853-2863, May 2021.
- [43] J. Friedman et al. *The elements of statistical learning*. Springer series in statistics New York, 2001, vol. 1, no. 10.
- [44] A. Massa and M. Salucci, "On the design of complex EM devices and systems through the System-by-Design paradigm: A framework for dealing with the computational complexity," *IEEE Trans. Antennas Propag.*, vol. 70, no. 2, pp. 1328-1343, Feb. 2022.
- [45] M. J. Burfeindt, T. J. Colgan, R. O. Mays, J. D. Shea, N. Behdad, B. D. Van Veen, and S. C. Hagness, "MRI-derived 3-D-printed breast phantom for microwave breast imaging validation," *IEEE Antennas Wireless Propag. Lett.*, vol. 11, pp. 1610-1613, Dec. 2012.

- [46] M. Solis-Nepote, T. Reimer, and S. Pistorius, "An air-operated bistatic system for breast microwave radar imaging: Pre-clinical validation," *2019 41st IEEE Annu. Int. Conf. Eng. Med. Biol. Soc. (EMBC)*, 2019, pp. 1859-1862.
- [47] A. I. J. Forrester, A. Sobester, and A. J. Keane, *Engineering Design via Surrogate Modelling: A Practical Guide*. Hoboken, NJ, USA: Wiley, 2008.
- [48] S. N. Lophaven, H. B. Nielsen, and J. Sondergaard, "Dace: A MATLAB Kriging toolbox," Dept. Informat. Math. Model., Tech. Univ. Denmark, Lyngby, Denmark, Tech. Rep. IMM-TR-2002-12, 2002.
- [49] C. J. D'Orsi, E. A. Sickles, E. B. Mendelson, and E. A. Morris, *ACR BI-RADS Atlas: Breast Imaging Reporting and Data System*. American College of Radiology, 2013.
- [50] D. O'Loughlin, B. L. Oliveira, A. Santorelli, E. Porter, M. Glavin, E. Jones, M. Popovic, and M. O'Halloran, "Sensitivity and specificity estimation using patient-specific microwave imaging in diverse experimental breast phantoms," *IEEE Trans. Med. Imaging*, vol. 38, no. 1, pp. 303-311, Jan. 2019.
- [51] A. Martellosio, M. Bellomi, M. Pasian, M. Bozzi, L. Perregrini, A. Mazzanti, F. Svelto, P. E. Summers, G. Renne, and L. Preda, "Dielectric properties characterization from 0.5 to 50 GHz of breast cancer tissues," *IEEE Trans. Microw. Theory Techn.*, vol. 65, no. 3, pp. 998-1011, Mar. 2017.
- [52] E. Zastrow, S. K. Davis, M. Lazebnik, F. Kelcz, B. D. Van Veen, and S. C. Hagness, "Development of anatomically realistic numerical breast phantoms with accurate dielectric properties for modeling microwave interactions with the human breast," *IEEE Trans. Biomed. Eng.*, vol. 55, no. 12, pp. 2792-2800, Dec. 2008.
- [53] A-Info, "LB-20200 Broadband Horn Antenna Specifications". Accessed: Oct. 12, 2022. [Online]. Available: http://ainfoinc.com.cn/en/pro_pdf/new_products/antenna/Broadband%20Horn%20Antenna/tr_LB-20200.pdf

- [54] U. Veronesi, B. Salvadori, A. Luini, A. Banfi, R. Zucali, M. Del Vecchio, R. Saccozzi, E. Beretta, P. Boracchi, G. Farante, V. Galimberti, G. Mezzanotte, V. Sacchini, S. Tana, and E. Marubini, "Conservative treatment of early breast cancer. Long-term results of 1232 cases treated with quadrantectomy, axillary dissection, and radiotherapy," *Ann. Surg.*, vol. 211, no. 3, pp. 250-259, Mar. 1990.
- [55] T. Reimer and S. Pistorius, "The diagnostic performance of machine learning in breast microwave sensing on an experimental dataset," *IEEE J. Electromagn. RF Microw. Med. Biol.*, vol. 6, no. 1, pp. 139-145, Mar. 2022.
- [56] S. S. Garud, I. A. Karimi, and M. Kraft, "Design of computer experiments: a review," *Comput. Chem. Eng.*, vol. 106, pp. 71-95, May 2017.
- [57] P. van den Berg and R. Kleinman, "A contrast source inversion method," *Inverse Probl.*, vol. 13, no. 6, pp. 1607-1620, Jul. 1997.
- [58] T. Reimer, J. Krenkevich, and S. Pistorius, "An open-access experimental dataset for breast microwave imaging," *2020 14th European Conf. Antennas Propag. (EuCAP)*, 2020, pp. 1-5.

FIGURE CAPTIONS

- **Figure 1.** Sketch of the geometry of (a) the 2-D microwave breast imaging setup and (b) the *Actual*, the *Reference*, and the *Differential* scattering scenarios.
- **Figure 2.** *Illustrative Example ("Ideal" Breast Phantom, $\varepsilon_B = 22.4$, $\sigma_B = 1.26$ [S/m], $\varepsilon_N = 16.5$, $\sigma_N = 0.60$ [S/m], $\varepsilon_\Psi = 59.3$, $\sigma_\Psi = 1.54$ [S/m])* - Distributions of the relative permittivity (a)(c) and the conductivity (b)(d) for (a)(b) the *Reference* and (c)(d) the *Actual* scenarios.
- **Figure 3.** *Illustrative Example ("Ideal" Breast Phantom, $f = 1.3$ [GHz], $\varepsilon_B = 22.4$, $\sigma_B = 1.26$ [S/m], $\varepsilon_N = 16.5$, $\sigma_N = 0.60$ [S/m], $\varepsilon_\Psi = 59.3$, $\sigma_\Psi = 1.54$ [S/m], $SNR = 100$ [dB])* - Plots of (a) the evolution of the differential data cost function, Φ_i , versus the iteration index, i , and (b) the total reconstruction error, Ξ_{tot} vs. execution time, Δt .
- **Figure 4.** *Illustrative Example ("Ideal" Breast Phantom, $f = 1.3$ [GHz], $\varepsilon_B = 22.4$, $\sigma_B = 1.26$ [S/m], $\varepsilon_N = 16.5$, $\sigma_N = 0.60$ [S/m], $\varepsilon_\Psi = 59.3$, $\sigma_\Psi = 1.54$ [S/m], $SNR = 100$ [dB])* - Profiles of (a)(c)(e) the relative permittivity and (b)(d)(f) the conductivity retrieved by (a)(b) the *SbD*, (c)(d) the *EA*, and (e)(f) the *DA* methods.
- **Figure 5.** *Numerical Results ("Segmented" Breast Phantom, XD Tissues (Tab. I), $f = 1.3$ [GHz], $\varepsilon_\Psi = 59.3$, $\sigma_\Psi = 1.54$ [S/m], $SNR = 100$ [dB])* - Profiles of (a)(c) the relative permittivity and (b)(d) the conductivity of the (a)(b) actual and (c)(d) the *SbD*-retrieved scenarios.
- **Figure 6.** *Numerical Results ("Segmented" Breast Phantom, XD Tissues (Tab. I), $f = 1.3$ [GHz], $\varepsilon_\Psi = 59.3$, $\sigma_\Psi = 1.54$ [S/m], $SNR \in [10, 100]$ [dB])* - Plots of (a) the total, (b) the internal, (c) the external reconstruction errors, and (d) the execution time as a function of the *SNR*.
- **Figure 7.** *Numerical Results ("Segmented" Breast Phantom, XD Tissues (Tab. I), $f = 1.3$ [GHz], $\varepsilon_\Psi = 59.3$, $\sigma_\Psi = 1.54$ [S/m], $SNR = 20$ [dB])* - Profiles of (a)(c)(e) the relative permittivity and (b)(d)(f) the conductivity retrieved by the (a)(b) *SbD*, (c)(d) the *EA*, and (e)(f) the *DA* methods.

- **Figure 8.** *Numerical Results (“Segmented” Breast Phantom, $f = 1.3$ [GHz], $\varepsilon_{\Psi} = 59.3$, $\sigma_{\Psi} = 1.54$ [S/m], $SNR = 100$ [dB]; *SbD* inversion) - Total, internal, and external reconstruction errors.*
- **Figure 9.** *Numerical Results (“Segmented” Breast Phantom, $f = 1.3$ [GHz], $\varepsilon_{\Psi} = 59.3$, $\sigma_{\Psi} = 1.54$ [S/m], $SNR = 100$ [dB]) - Maps of (a)(c)(e)(g)(i)(m) the actual and (b)(d)(f)(h)(l)(n) the retrieved profiles of the (a)(b)(e)(f)(i)(l) relative permittivity and (c)(d)(g)(h)(m)(n) conductivity when imaging breast phantoms belonging to the (a)-(d) “fatty”, (e)-(h) “scattered”, and (i)-(n) “HD” categories.*
- **Figure 10.** *Numerical Results (“Segmented” Breast Phantom, *XD Tissues* (Tab. I), $f = 1.3$ [GHz], $\varepsilon_{\Psi}^{(nom)} = 59.3$, $\sigma_{\Psi}^{(nom)} = 1.54$ [S/m], $SNR = 100$ [dB]) - Total, internal, and external reconstruction error versus δ .*
- **Figure 11.** *Numerical Results (“Segmented” Breast Phantom, *XD Tissues* (Tab. I), $f = 1.3$ [GHz], $\varepsilon_{\Psi}^{(nom)} = 59.3$, $\sigma_{\Psi}^{(nom)} = 1.54$ [S/m], $SNR = 100$ [dB]) - Maps of (a)(b)(e)(f) the actual and (c)(d)(g)(h) the reconstructed profiles of the (a)-(d) relative permittivity and (e)-(h) conductivity when (a)(c)(e)(g) $\delta = -10\%$ and (b)(d)(f)(h) $\delta = +10\%$.*
- **Figure 12.** *Numerical Results (“Full” Breast Phantom, *Scattered Tissues*) - Maps of (a)(c)(e) the relative permittivity and (b)(d)(f) the conductivity profiles for the (a)(b) full, (c)(d) segmented, and (e)(f) constant *prior* knowledge on the reference scenario.*
- **Figure 13.** *Numerical Results (“Full” Breast Phantom, *Scattered Tissues* (Tab. I), $f = 1.3$ [GHz], $\varepsilon_{\Psi} = 59.3$, $\sigma_{\Psi} = 1.54$ [S/m], $SNR = 100$ [dB]) - Maps of (a)(b) the actual and (c)-(h) the retrieved (a)(c)(e)(g) relative permittivity and (b)(d)(f)(h) conductivity profiles when considering the (c)(d) full (*FP*), (e)(f) segmented (*SP*), or (g)(h) constant (*CP*) *prior* knowledge on the reference scenario.*
- **Figure 14.** *Experimental Results (UM-BMID Dataset [25][58], $\rho_{\Psi} = 1.50$ [cm], $f = 2.0$ [GHz]) - Maps of (a)(b) the actual and (c)-(h) the retrieved (a)(c)(e)(g) relative permittivity and (b)(d)(f)(h) conductivity profiles by the (c)(d) *SbD*, (e)(f) *EA*, and (g)(h) *DA*.*

- **Figure 15.** *Experimental Results (UM-BMID Dataset [25][58], $\rho_{\Psi} = 0.75$ [cm], $f = 2.0$ [GHz])* - Maps of (a)(b) the actual and (c)-(h) the retrieved (a)(c)(e)(g) relative permittivity and (b)(d)(f)(h) conductivity profiles by the (c)(d) *SbD*, (e)(f) *EA*, and (g)(h) *DA*.

TABLE CAPTIONS

- **Table I.** *Numerical Results (Segmented Breast Phantom, $f = 1.3$ [GHz])* - Description of the *MRI*-derived piece-wise constant phantoms [17].
- **Table II.** *Numerical Results (“Full” Breast Phantom, Scattered Tissues, $f = 1.3$ [GHz], $\varepsilon_{\Psi} = 59.3$, $\sigma_{\Psi} = 1.54$ [S/m], $SNR = 100$ [dB])* - Reconstruction errors and execution time.
- **Table III.** *Numerical Results (“Full” Breast Phantom, Scattered Tissues, $f = 1.3$ [GHz], $\varepsilon_{\Psi} = 59.3$, $\sigma_{\Psi} = 1.54$ [S/m], $SNR = 100$ [dB]; *SbD* inversion)* - Error metrics.
- **Table IV.** *Experimental Results (UM-BMID Dataset [25][58], $f = 2.0$ [GHz])* - Reconstruction errors and execution time.
- **Table V.** *Experimental Results (UM-BMID Dataset [25][58], $f = 2.0$ [GHz])* - Breast tumor detection/localization indexes.

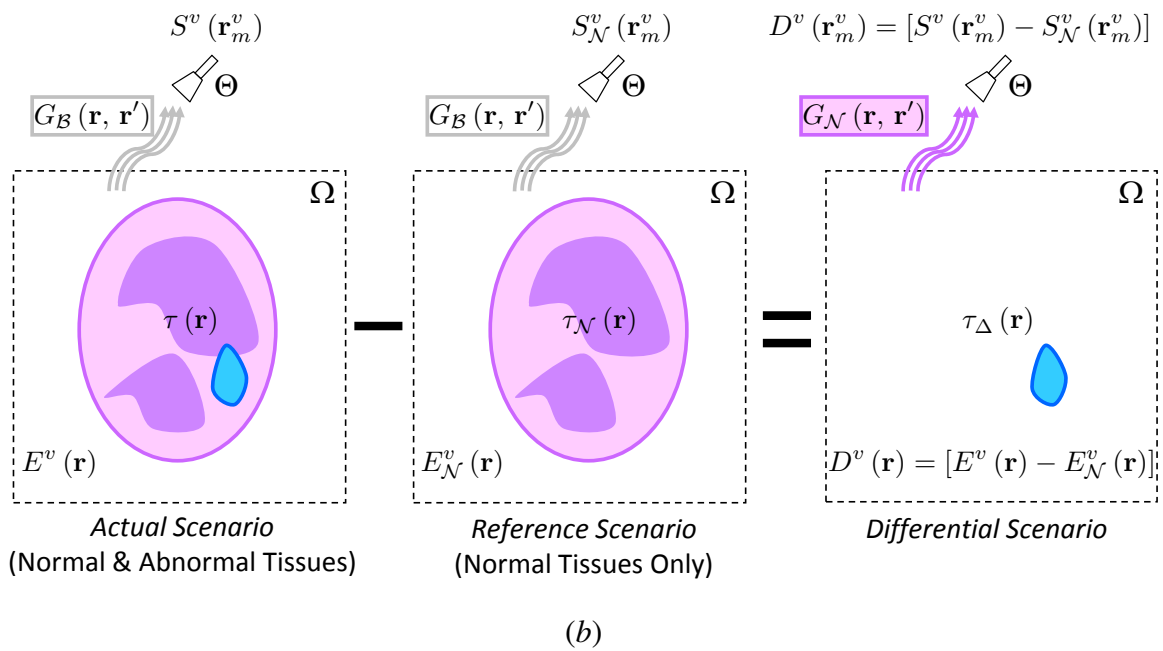
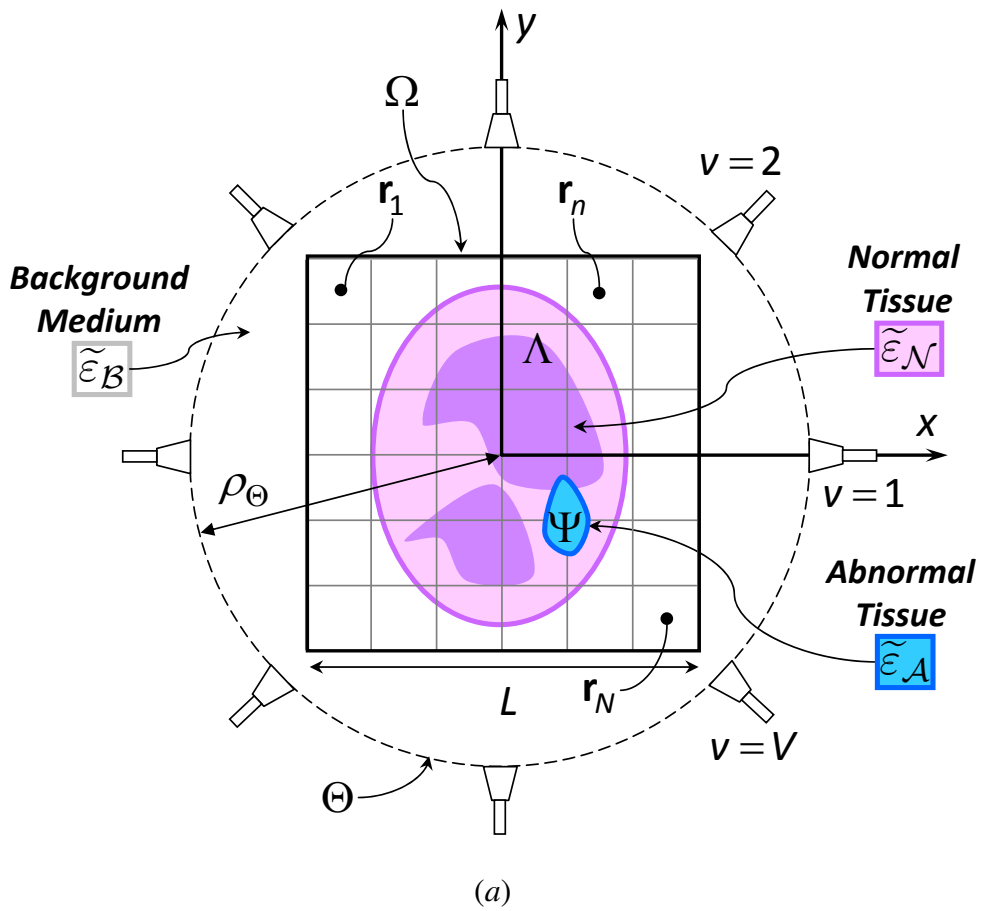


Fig. 1 - F. Zardi et al., “A Physics-Driven AI Approach ...”

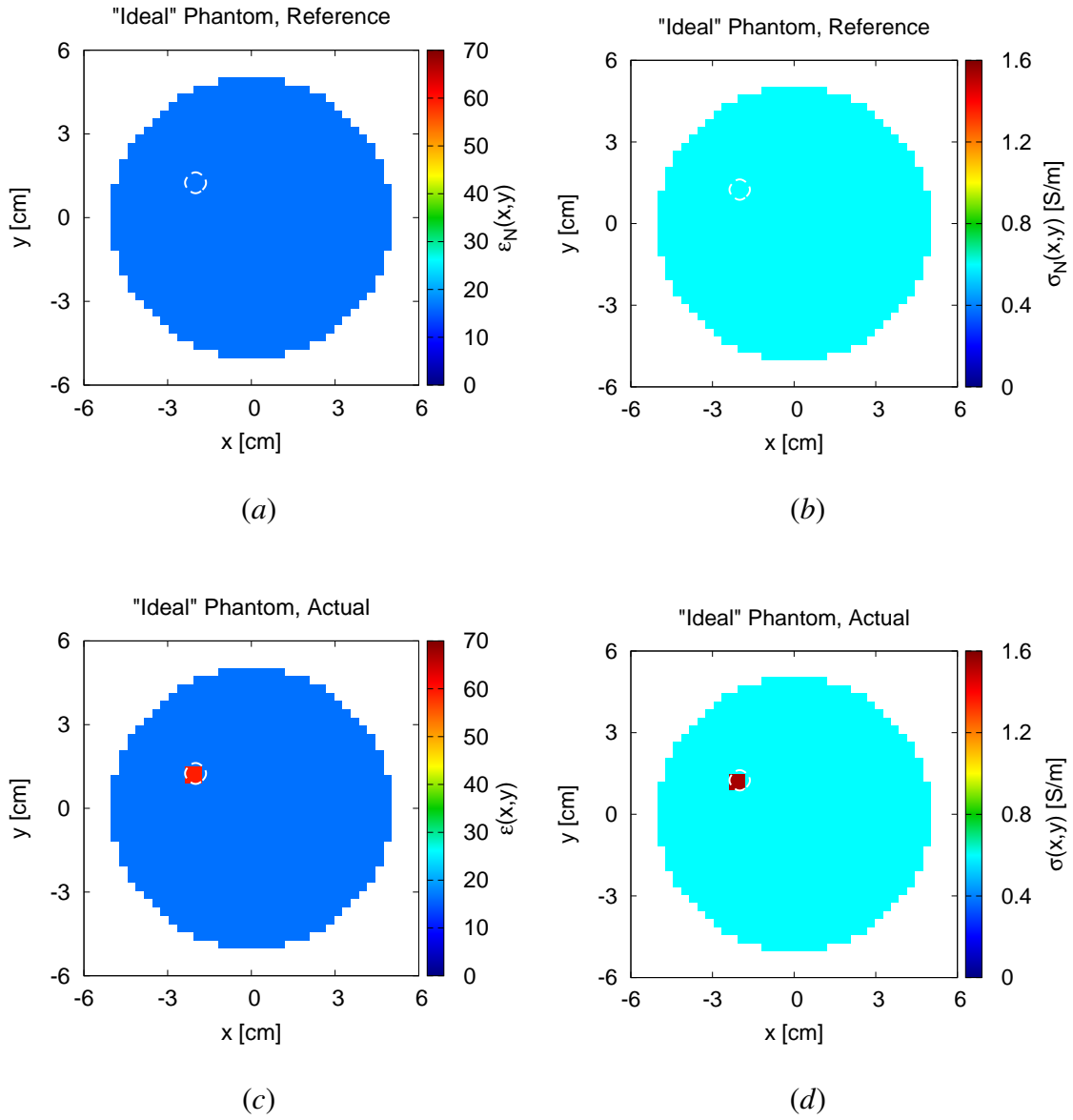
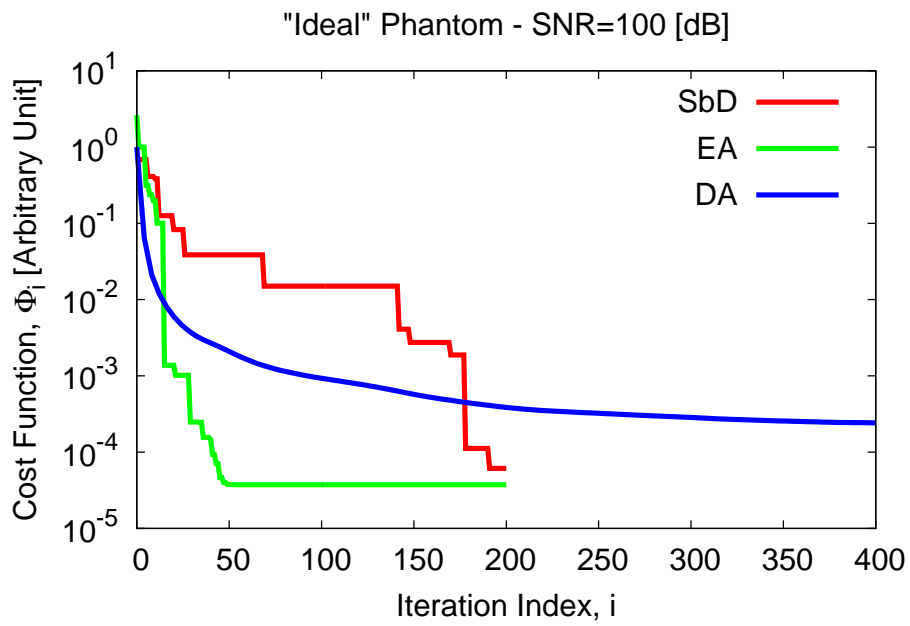
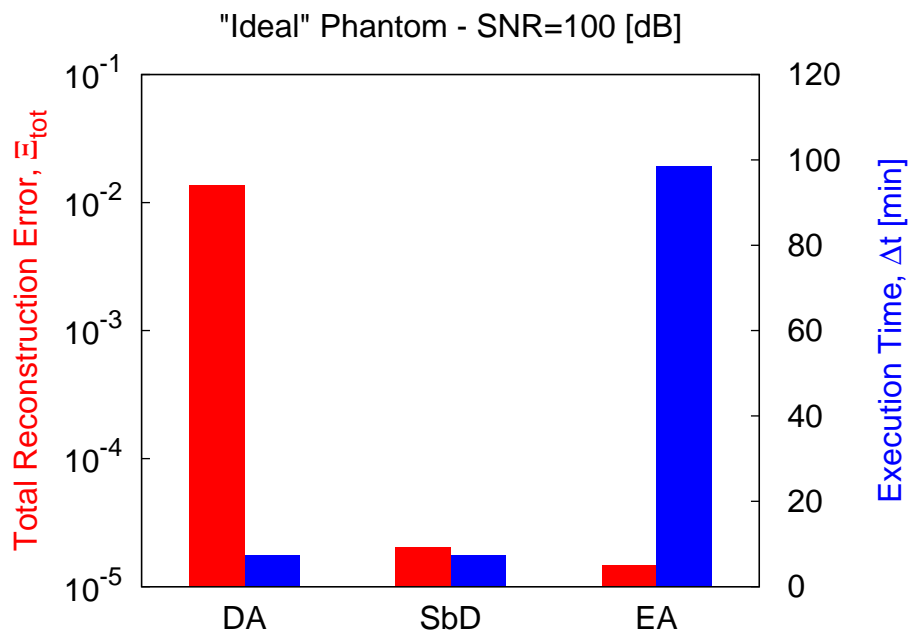


Fig. 2 - F. Zardi et al., “A Physics-Driven AI Approach ...”



(a)



(b)

Fig. 3 - F. Zardi et al., "A Physics-Driven AI Approach ..."

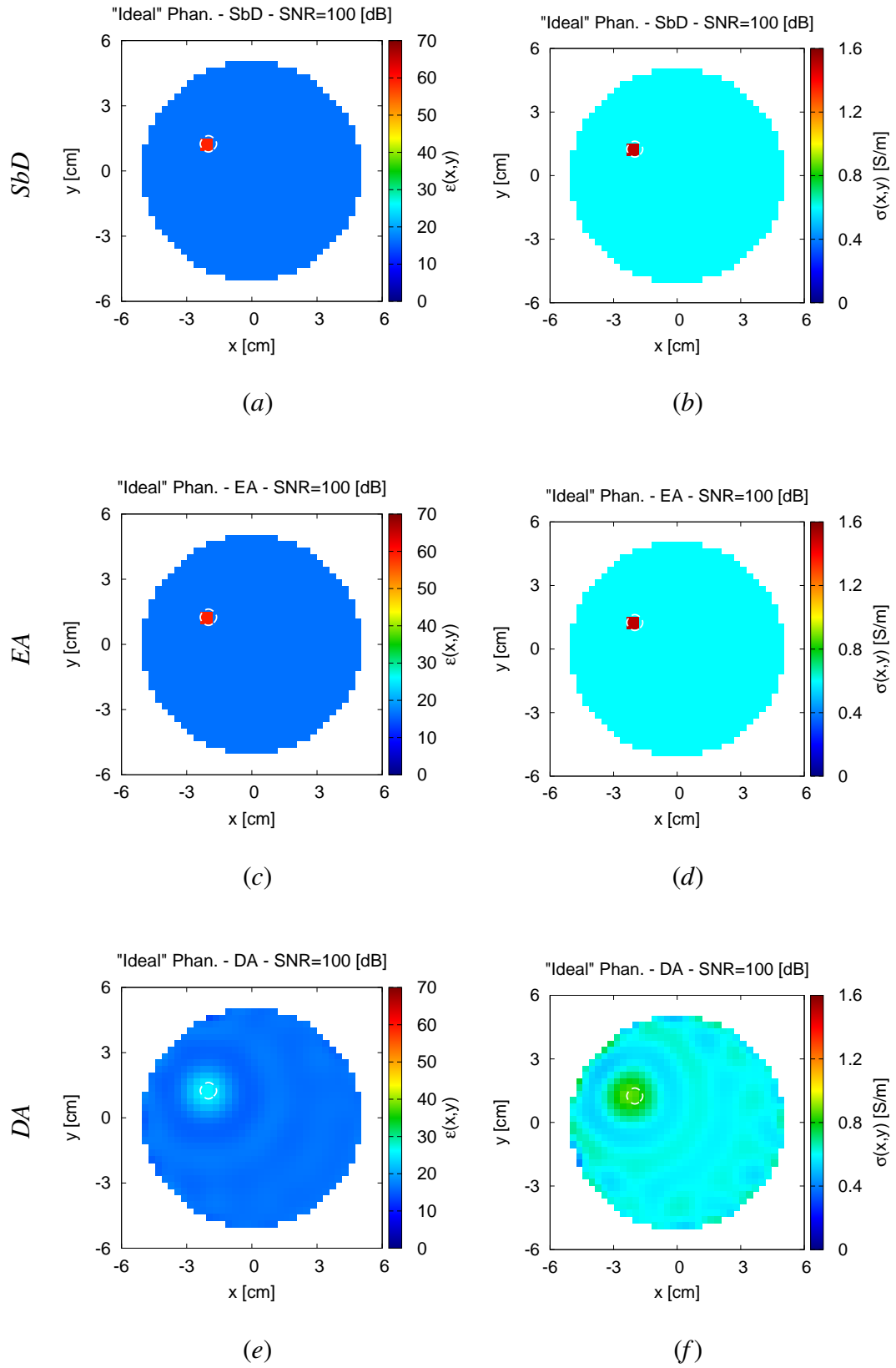


Fig. 4 - F. Zardi et al., "A Physics-Driven AI Approach ..."

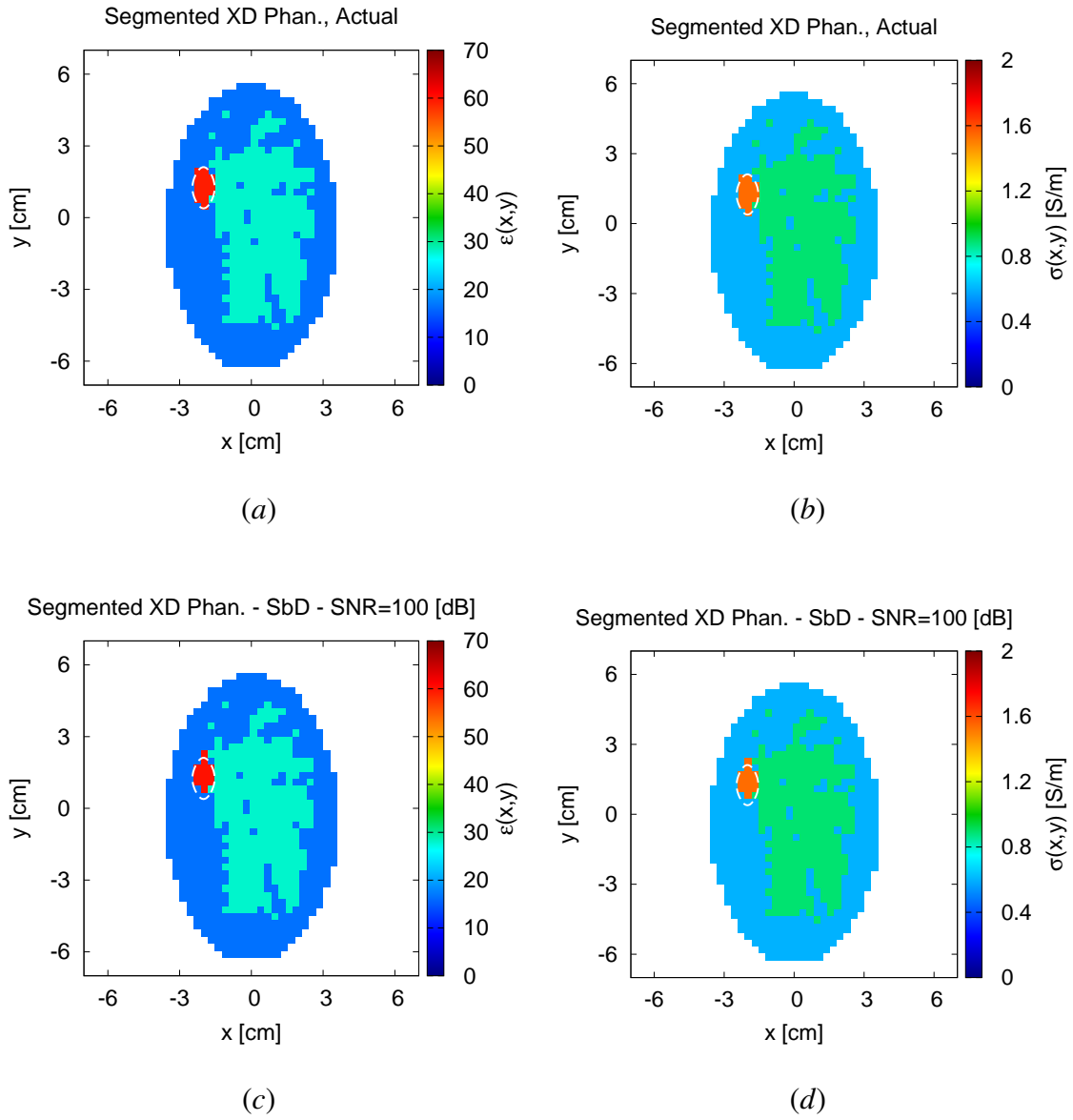
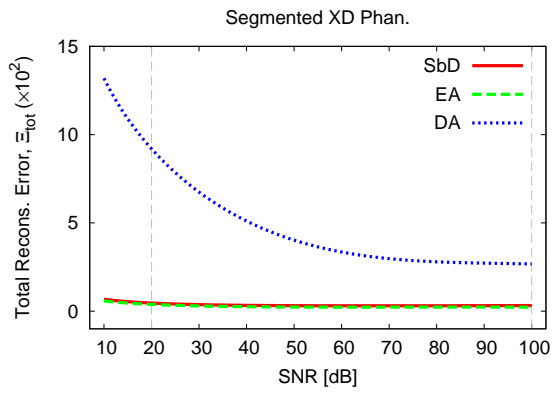
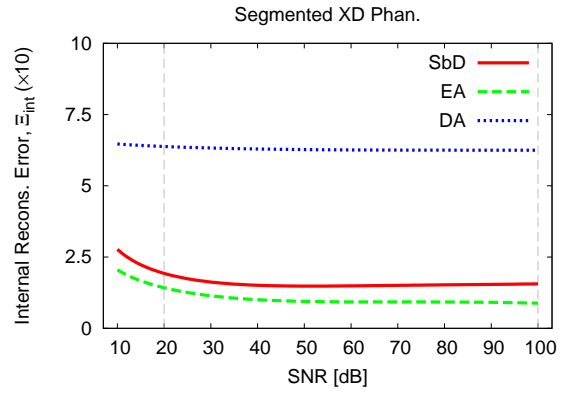


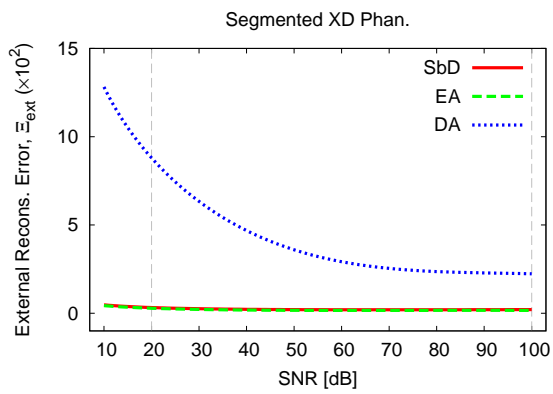
Fig. 5 - F. Zardi et al., “A Physics-Driven AI Approach ...”



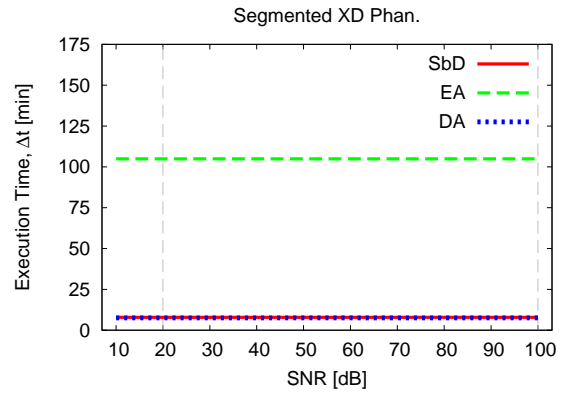
(a)



(b)



(c)



(d)

Fig. 6 - F. Zardi et al., "A Physics-Driven AI Approach ..."

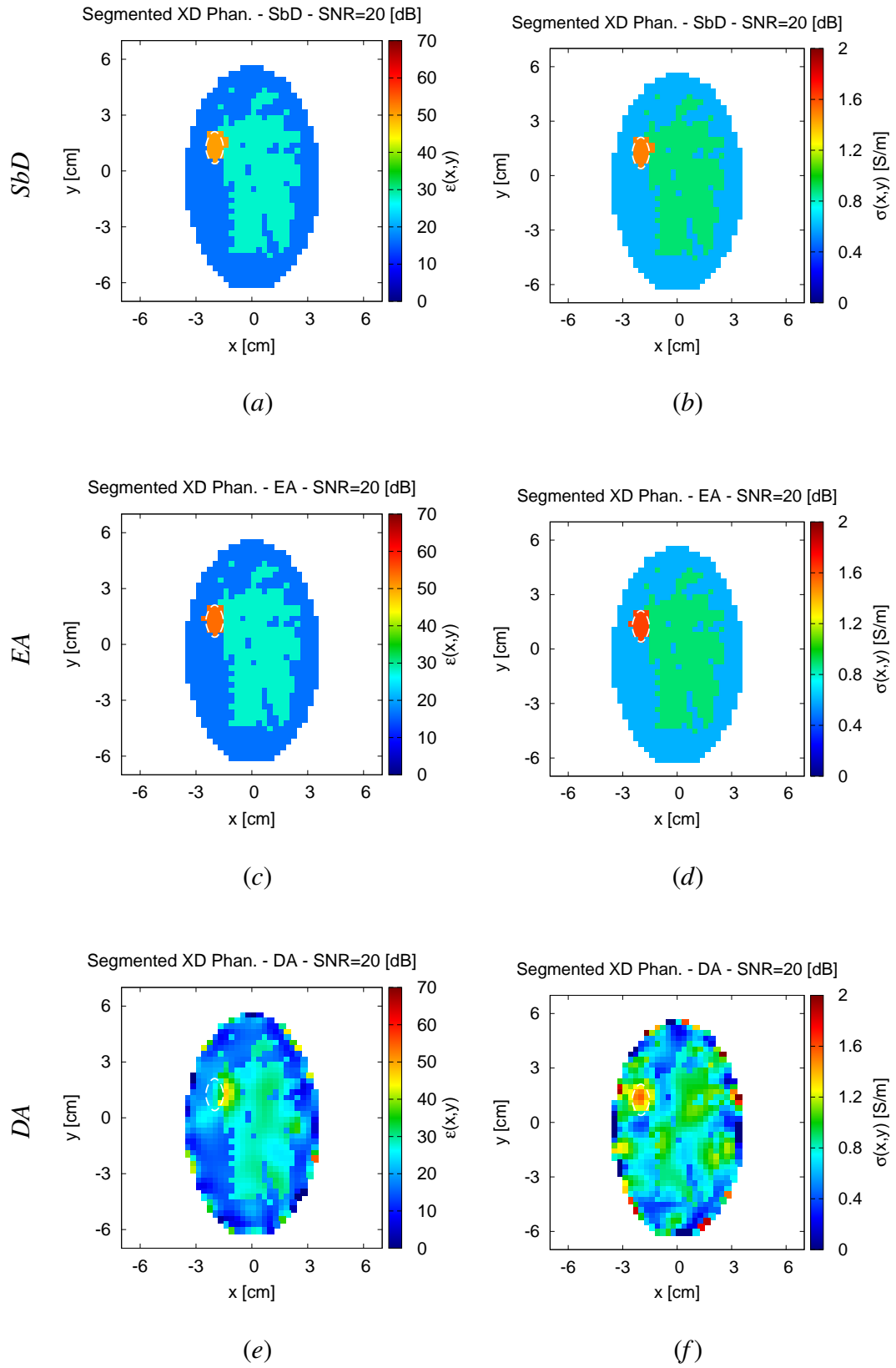


Fig. 7 - F. Zardi et al., “A Physics-Driven AI Approach ...”

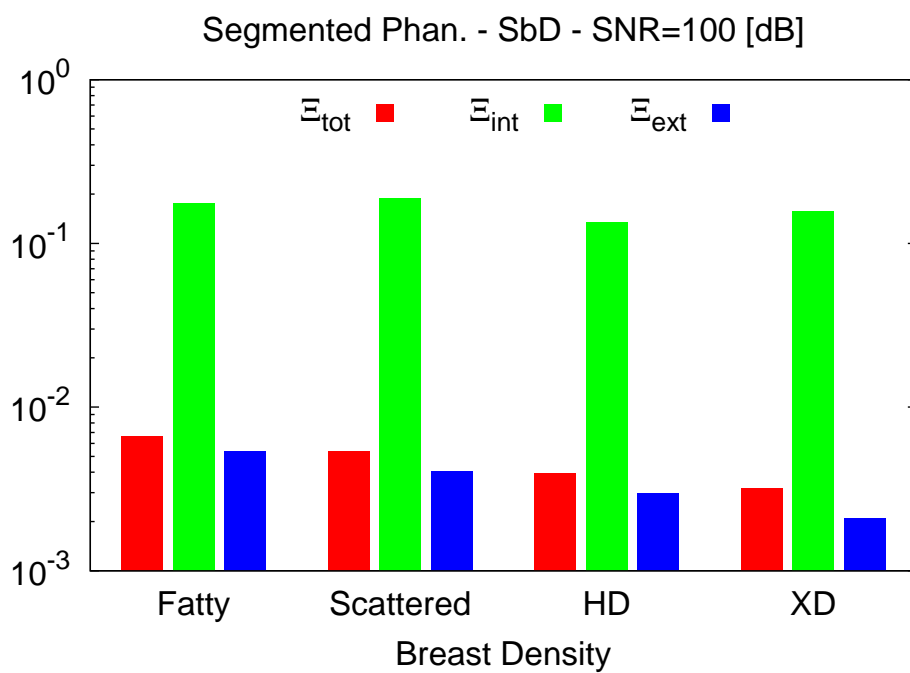
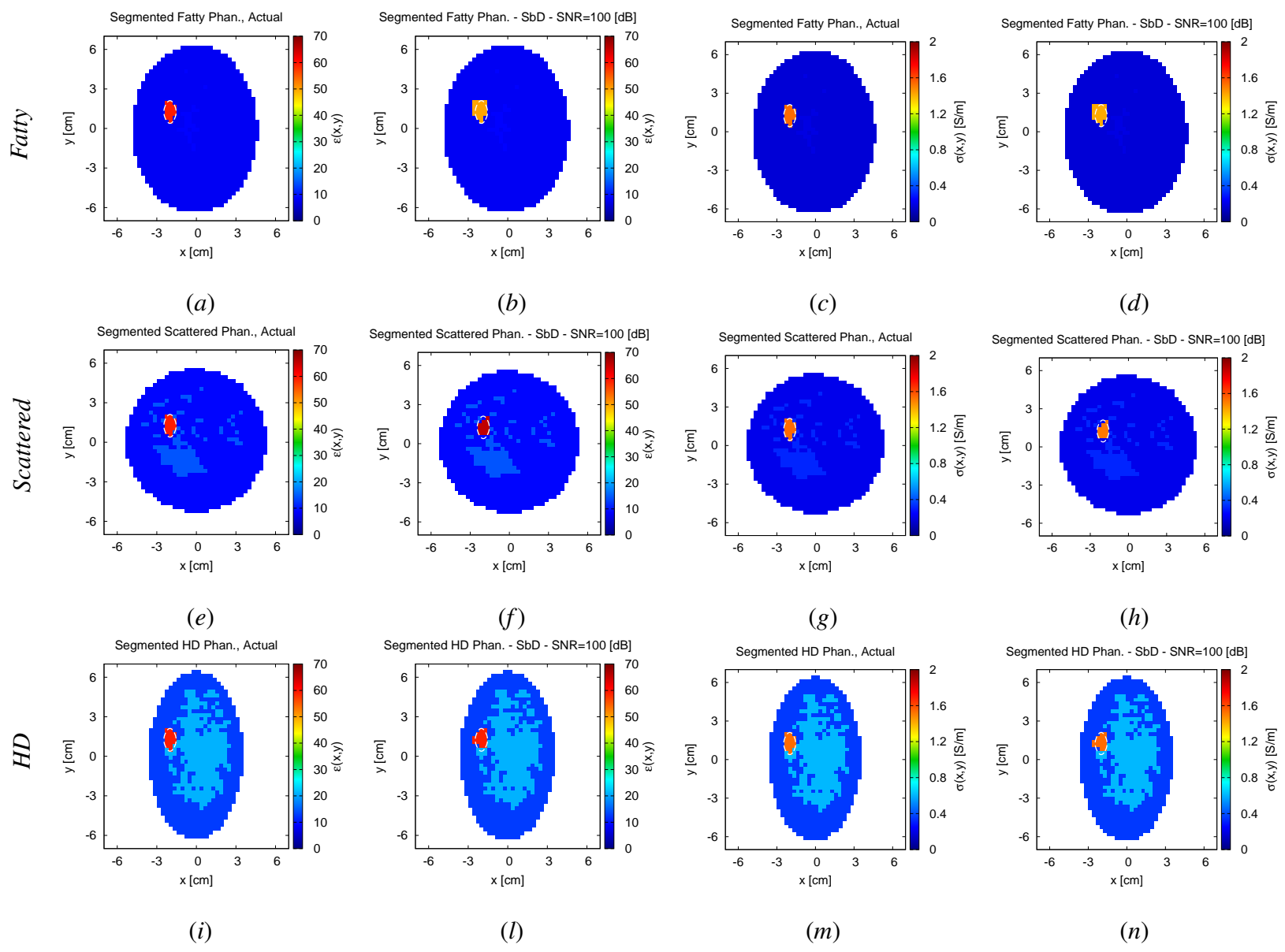


Fig. 8 - F. Zardi et al., “A Physics-Driven AI Approach ...”

Fig. 9 - F. Zardi et al., "A Physics-Driven AI Approach ..."



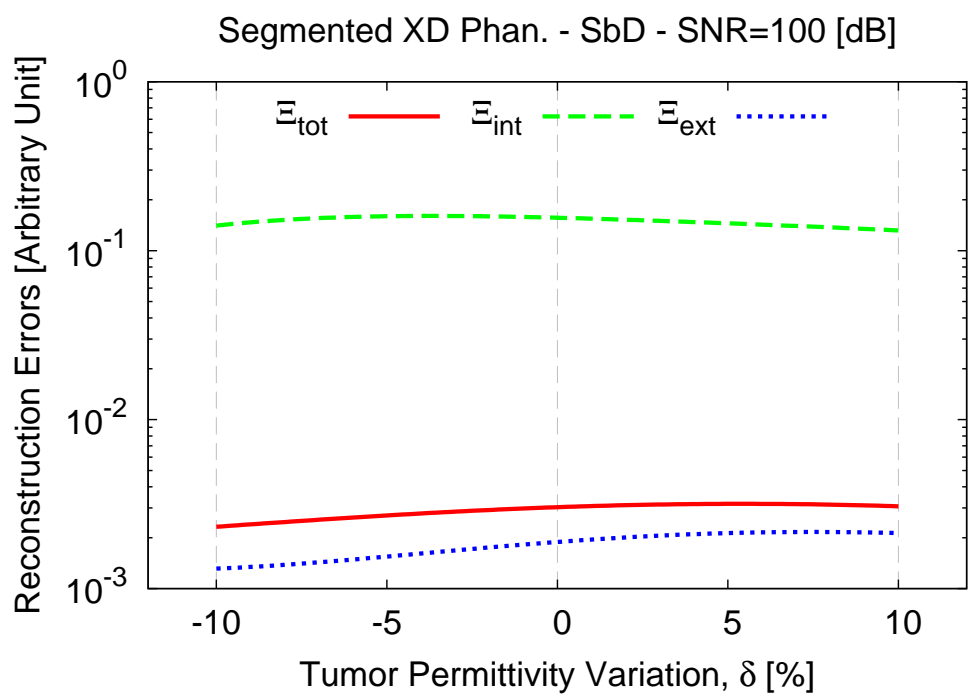


Fig. 10 - F. Zardi et al., "A Physics-Driven AI Approach ..."

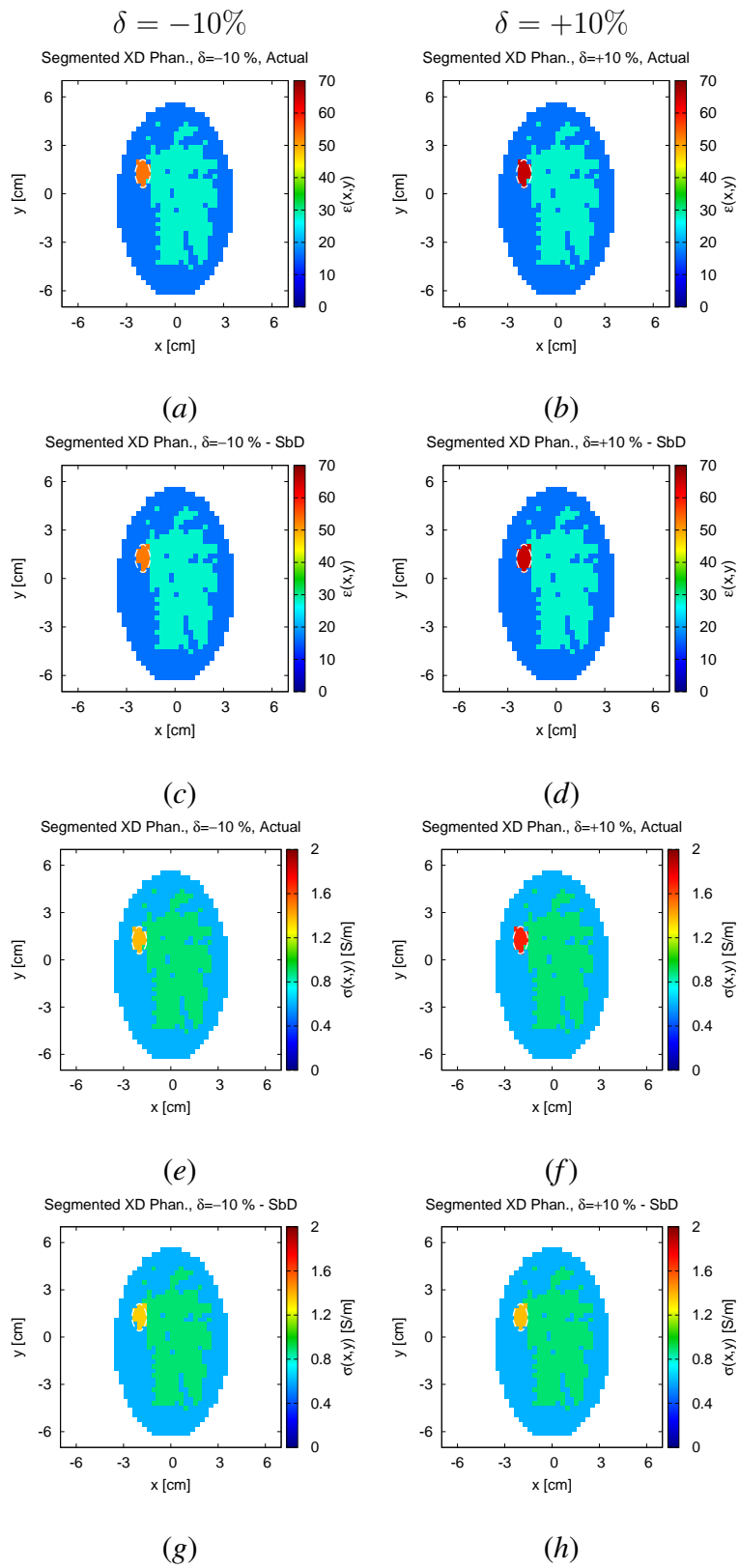


Fig. 11 - F. Zardi et al., “A Physics-Driven AI Approach ...”

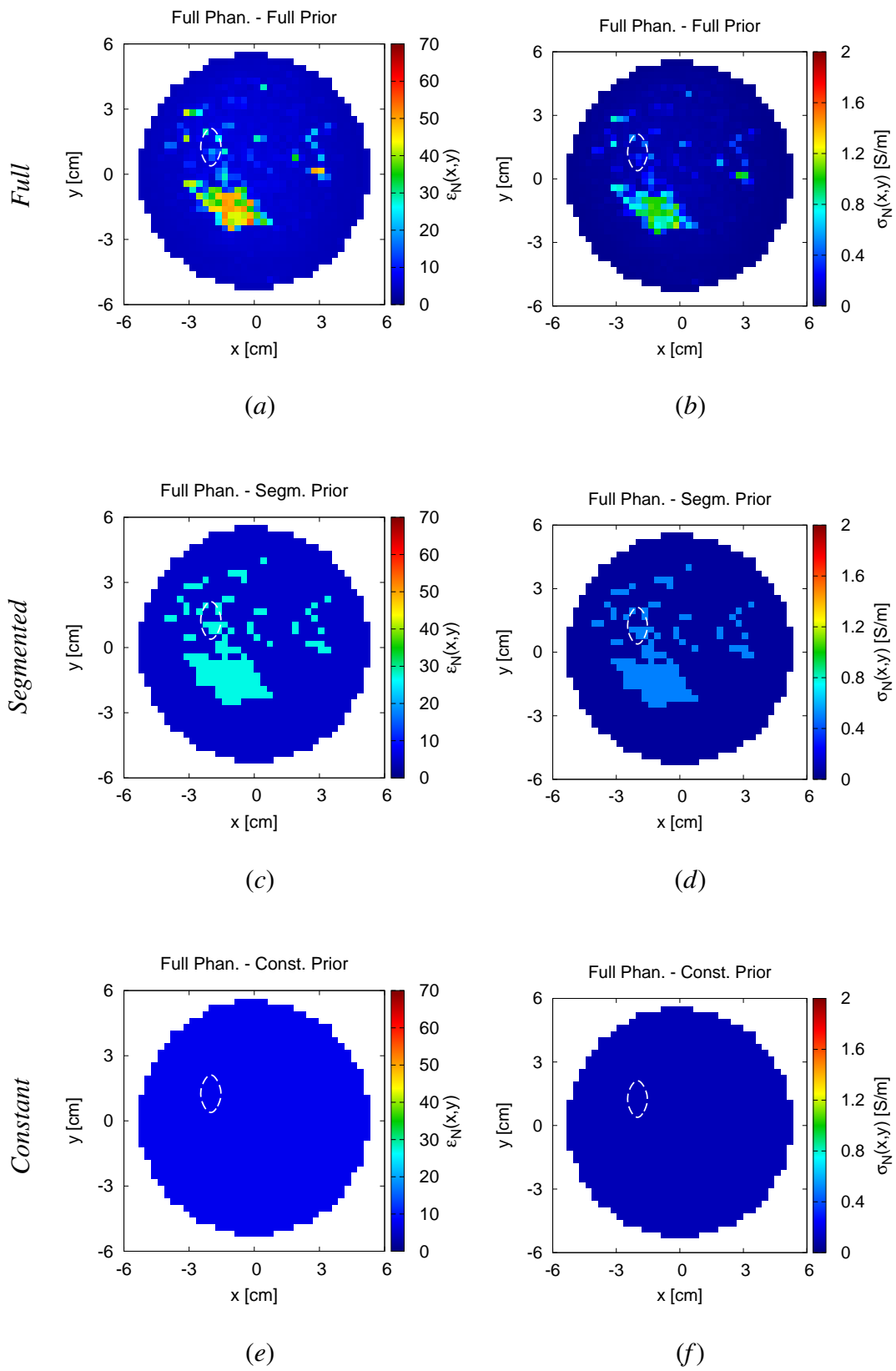


Fig. 12 - F. Zardi et al., “A Physics-Driven AI Approach ...”

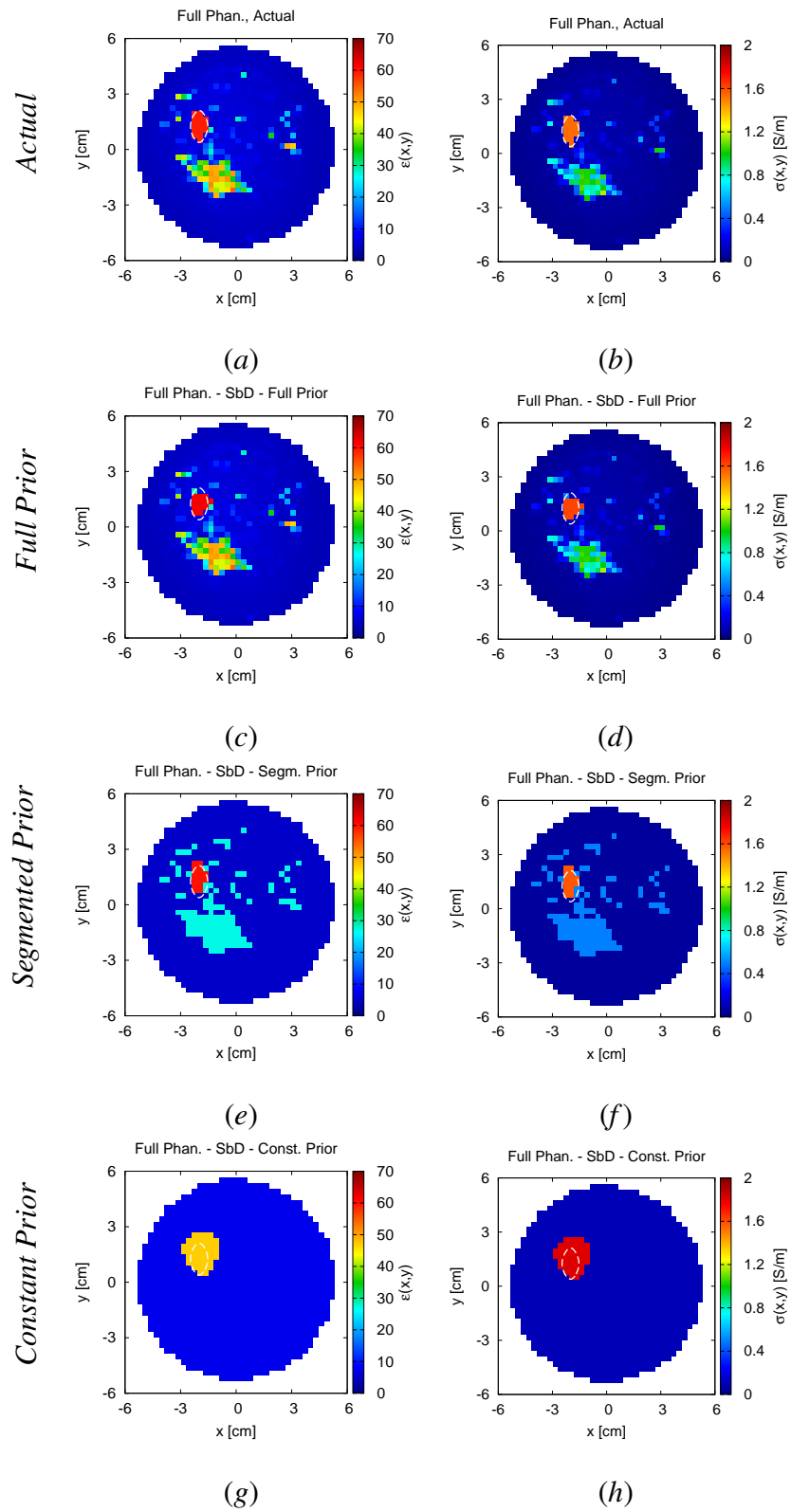


Fig. 13 - F. Zardi et al., “A Physics-Driven AI Approach ...”

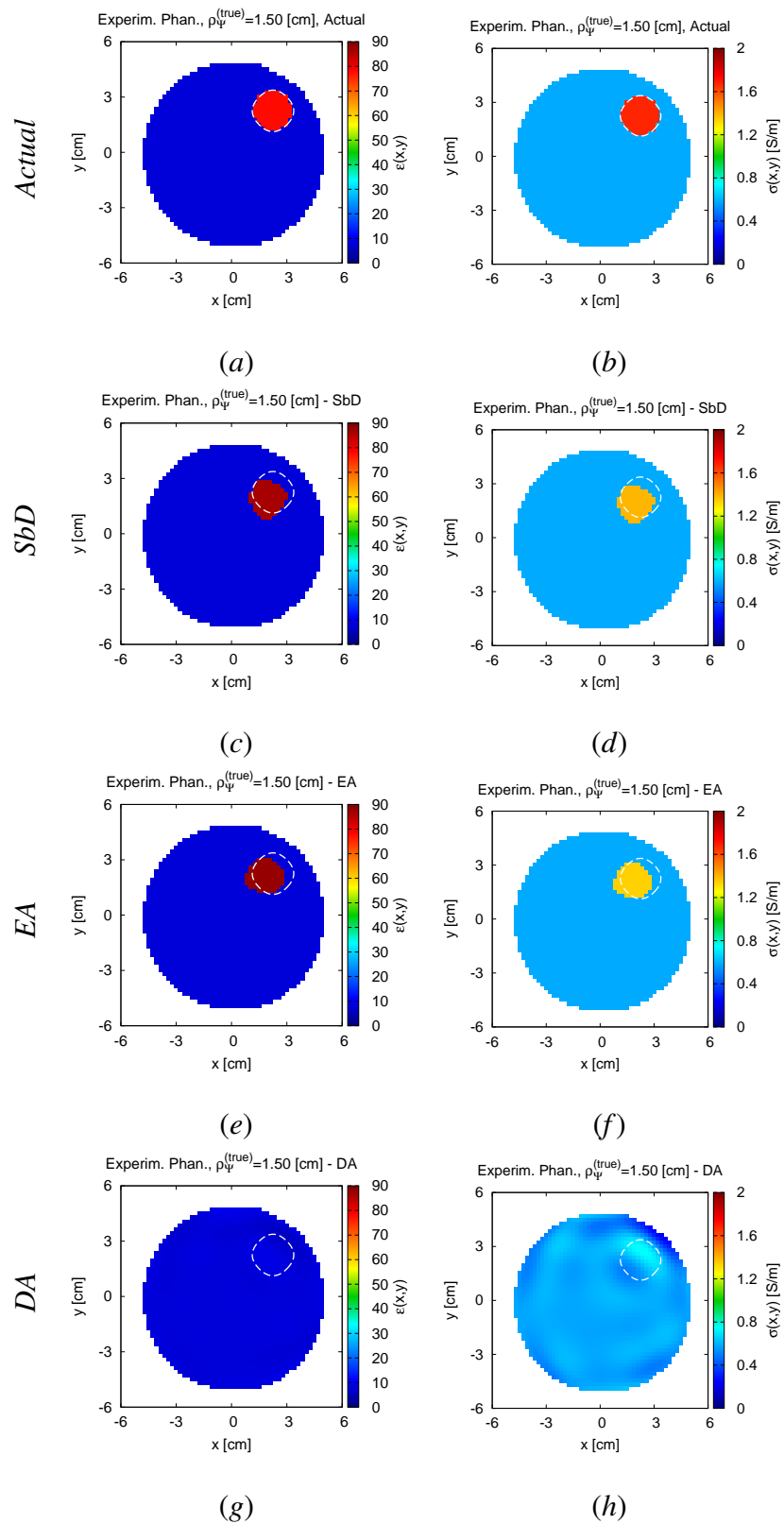


Fig. 14 - F. Zardi et al., “A Physics-Driven AI Approach ...”

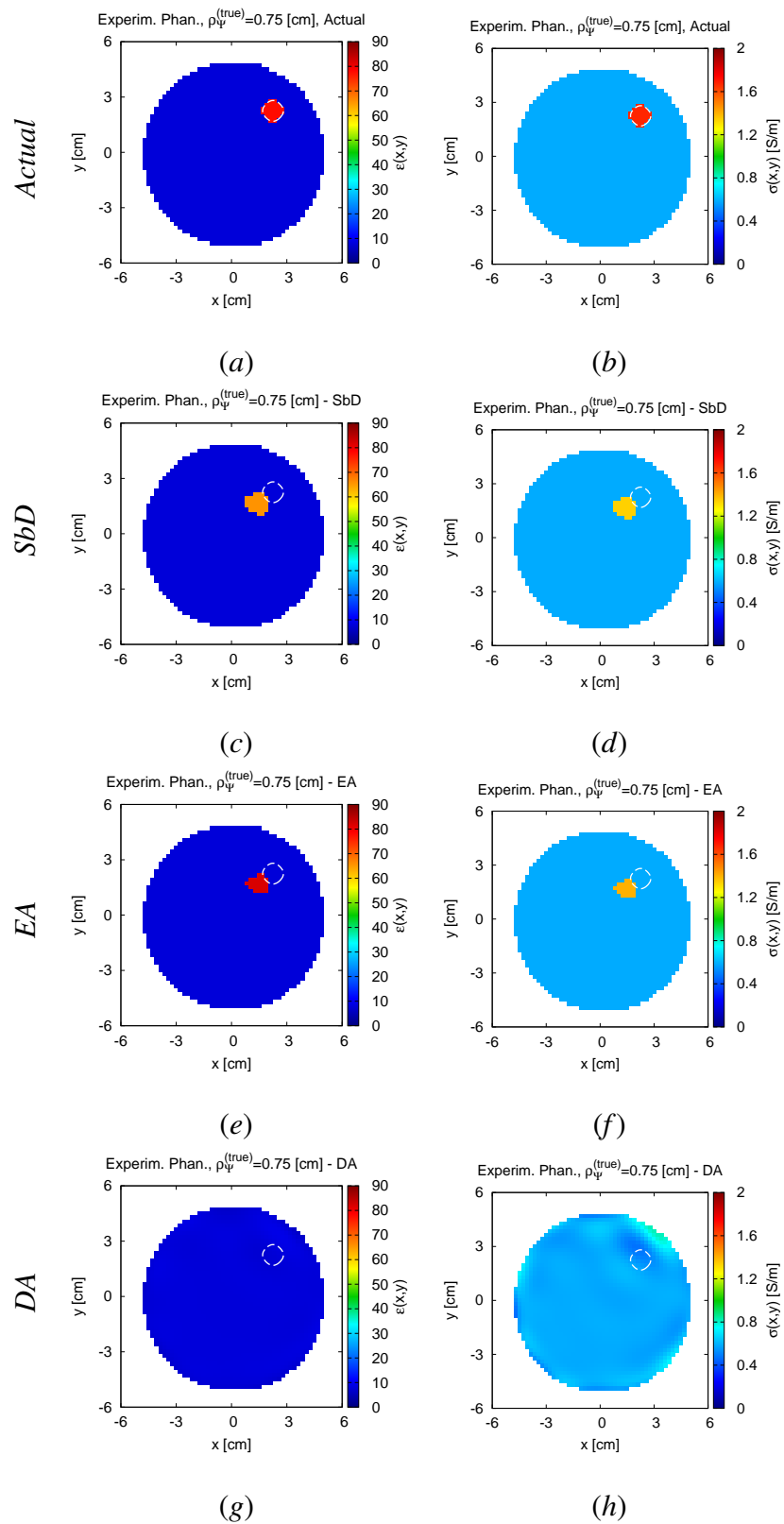


Fig. 15 - F. Zardi et al., “A Physics-Driven AI Approach ...”

| <i>UWCEM</i> <i>ID</i> | <i>Breast</i> <i>Density</i> | <i>Adipose</i> | | <i>Fibroglandular</i> | | <i>Background</i> | |
|---------------------------|---------------------------------|--------------------------|------------------------------|--------------------------|------------------------------|--------------------------|------------------------------|
| | | $\epsilon_{\mathcal{N}}$ | $\sigma_{\mathcal{N}}$ [S/m] | $\epsilon_{\mathcal{N}}$ | $\sigma_{\mathcal{N}}$ [S/m] | $\epsilon_{\mathcal{B}}$ | $\sigma_{\mathcal{B}}$ [S/m] |
| 012304 | <i>XD</i> | 16.5 | 0.60 | 28.0 | 0.89 | 22.4 | 1.26 |
| 080304 | <i>HD</i> | 12.8 | 0.36 | 21.0 | 0.61 | 22.4 | 1.26 |
| 012204 | Scattered | 9.0 | 0.21 | 14.5 | 0.32 | 13.6 | 0.87 |
| 071904 | Fatty | 8.0 | 0.17 | 8.8 | 0.195 | 13.6 | 0.87 |

Table I - F. Zardi et al., “A Physics-Driven AI Approach ...”

| <i>Method</i> | Ξ_{tot} | Ξ_{int} | Ξ_{ext} | Δt [min] |
|---------------|-----------------------|-----------------------|-----------------------|------------------|
| <i>SbD</i> | 3.48×10^{-3} | 1.89×10^{-1} | 3.72×10^{-3} | 12 |
| <i>EA</i> | 3.46×10^{-3} | 1.29×10^{-1} | 3.69×10^{-3} | 164 |
| <i>DA</i> | 7.66×10^{-2} | 7.53×10^{-1} | 7.17×10^{-2} | 12 |

Table II - F. Zardi et al., “A Physics-Driven AI Approach ...”

| <i>Prior Knowledge</i> | Ξ_{tot} | Ξ_{int} | Ξ_{ext} |
|-------------------------|-----------------------|-----------------------|-----------------------|
| Full (<i>FP</i>) | 3.08×10^{-3} | 1.59×10^{-1} | 1.72×10^{-3} |
| Segmented (<i>SP</i>) | 4.16×10^{-3} | 1.71×10^{-1} | 3.31×10^{-3} |
| Constant (<i>CP</i>) | 3.63×10^{-2} | 1.90×10^{-1} | 3.52×10^{-2} |

Table III - F. Zardi et al., “A Physics-Driven *AI* Approach ...”

| <i>Method</i> | Ξ_{tot} | Ξ_{int} | Ξ_{ext} | Δt [min] |
|------------------------------------|-----------------------|-----------------------|-----------------------|------------------|
| $\rho_{\Psi}^{(true)} = 1.5$ [cm] | | | | |
| <i>SbD</i> | 2.23×10^{-2} | 3.19×10^{-1} | 1.80×10^{-2} | 21 |
| <i>EA</i> | 2.06×10^{-2} | 3.50×10^{-1} | 1.58×10^{-2} | 304 |
| <i>DA</i> | 2.51×10^{-2} | 8.86×10^{-1} | 1.27×10^{-2} | 21 |
| $\rho_{\Psi}^{(true)} = 0.75$ [cm] | | | | |
| <i>SbD</i> | 1.92×10^{-2} | 4.96×10^{-1} | 1.75×10^{-2} | 21 |
| <i>EA</i> | 1.86×10^{-2} | 4.72×10^{-1} | 1.68×10^{-2} | 295 |
| <i>DA</i> | 2.06×10^{-2} | 8.91×10^{-1} | 8.24×10^{-3} | 21 |

Table IV - F. Zardi et al., “A Physics-Driven AI Approach ...”

| | $\rho_{\Psi} = 1.5$ [cm] | | $\rho_{\Psi} = 0.75$ [cm] | |
|------------------|--------------------------|------------------|---------------------------|------------------|
| <i>Method</i> | ζ [cm] | <i>Detection</i> | ζ [cm] | <i>Detection</i> |
| <i>SbD</i> | 0.48 | Yes | 1.03 | Yes |
| <i>EA</i> | 0.45 | Yes | 0.96 | Yes |
| <i>DA</i> | 1.83 | Yes | 2.47 | No |
| <i>DAS</i> [25] | 1.00 | Yes | 3.76 | No |
| <i>DMAS</i> [25] | 1.01 | Yes | 3.76 | No |
| <i>ORR</i> [25] | 1.21 | Yes | 3.62 | No |

Table V - F. Zardi et al., “A Physics-Driven AI Approach ...”